A Digital Twin Approach for Fault Diagnosis in Distributed Photovoltaic Systems

Palak Jain, *Student Member, IEEE,* Jason Poon, *Student Member, IEEE,* Jai Prakash Singh, Costas Spanos, *Fellow, IEEE,* Seth R. Sanders, *Fellow, IEEE,* Sanjib Kumar Panda, *Senior Member, IEEE*

Abstract—**Rooftop and building-integrated distributed photovoltaic (PV) systems are emerging as key technologies for smart building applications. This paper presents the design methodology, mathematical analysis, simulation study, and experimental validation of a digital twin approach for fault diagnosis. We develop a digital twin that estimates the measurable characteristic outputs of a PV energy conversion unit (PVECU) in real-time. The PVECU constitutes a PV source and a source-level power converter. The fault diagnosis is performed by generating and evaluating an error residual vector, which is the difference between the estimated and measured outputs. A PV panel-level power converter prototype is built to demonstrate how the sensing, processing, and actuation capabilities of the converter can enable effective fault diagnosis in real-time. The experimental results show detection and identification of ten different faults in the PVECU. The time to fault detection in the power converter and the electrical sensors is less than 290 μs and the identification time is less than 4 ms. The time to fault detection and identification in the PV panel are less than 80 ms and 1.2 s, respectively. The proposed approach demonstrates higher fault sensitivity than that of existing approaches. It can diagnose a 20% drift in the electrical sensor gains and a 20% shading of a solar cell in the PV panel.**

Index Terms—**Fault diagnosis, fault location, estimation, solar power generation, converters**

I. INTRODUCTION

Photovoltaic (PV) energy conversion architectures based on panel or subpanel-level distributed power electronic converters are increasingly ubiquitous for rooftop and building-integrated PV (BIPV) systems [2]–[5]. The unique advantages of a distributed power electronic-based PV system include higher energy yield (particularly, in partial shading conditions), higher performance reliability, lower installation costs, plug-and-play operation, and enhanced system flexibility, modularity, and scalability [3], [6]–[8]. The building block of a distributed PV system can be referred to as a *PV energy conversion unit*

P. Jain and S. Panda are with the Department of Electrical and Computer Engineering at the National University of Singapore (NUS), Singapore 117583 (email: palakjain@u.nus.edu; sanjib.kumar.panda@nus.edu.sg).

J. P. Singh is with the Solar Energy Research Institute of Singapore, NUS, Singapore 117574 (email: jaiprakash.singh@nus.edu.sg).

J. Poon, C. Spanos, and S. Sanders are with the Department of Electrical Engineering and Computer Sciences at the University of California, Berkeley, CA 94720 USA (email: {jason, spanos, seth.sanders}@berkeley.edu).

(PVECU). The PVECU constitutes a PV source (e.g. a PV panel or a PV subpanel) and a source-level power converter.

The distributed PV systems are vulnerable to a variety of faults due to their complex outdoor installations, increased number of power electronic converters at the PV panel-level, harsh mission profiles, manufacturing defects, and aging. A comprehensive analysis of common failure modes that could occur in these PV systems and their impacts on performance and reliability are given in [9]–[11]. These failures degrade system performance, and endanger the safety and security of the buildings and its occupants. Moreover, these failures are difficult to locate and repair in building applications because rooftop and BIPV systems have a very large number of PVECUs which can be physically inaccessible due to complex installations (exacerbating maintenance and inspection that incur high cost). Thus, robust and cost-effective methods for ensuring their dependability and fault tolerance are necessary.

Strategies for fault diagnosis have been explored to improve dependability and fault tolerance of complex systems. Fault diagnosis is a monitoring scheme that is comprised of two functions: 1) fault detection (FD), which is a binary decision on the occurrence of a fault; and 2) fault identification (FI), which is the process of classifying the precise fault type [12]. The successful fault diagnosis in a distributed PV system enables online fault remediation, increasing its availability and decreasing its maintenance costs.

Prior works in the literature address fault diagnosis of various subcomponents of PV systems. For example, the authors in [13]–[15] investigate various fault diagnosis approaches for power electronic converters in PV systems. Similarly, the authors in [16]–[18] report various methodologies for PV panel fault diagnosis. However, there is a lack of research work towards a holistic fault diagnosis approach for a complete PVECU. Table I presents common failure modes of each subcomponent in the PVECU. The holistic fault diagnosis approach should, at a minimum, be able to detect and identify these failure modes.

Commercial PV monitoring solutions are available that provide web-based monitoring and use data analytics to detect a fault event [24], [25]. However, these solutions typically lack: 1) the ability to perform FI; 2) require high bandwidth communication for data acquisition and control; 3) require additional central processing units (CPUs); and 4) add latency in the diagnostics of system performance and faults.

This work applies the concept of a *digital twin* to develop a holistic fault diagnosis approach. A digital twin is a digital emulation of a physical system that estimates the

TABLE I
COMMON FAILURE MODES OF A PVECU.

COMPONENTS	COMMON FAILURE MODES
PV panel [11], [19], [20]	Soiling Continuous/repetitive partial shading conditions Cells breakage EVA browning Bypass diode failures Potential induced degradation (PID) Interconnect faults Internal faults related to PV shunt and series resistances
Power converter [21]–[23]	Switch open circuit Switch short circuit Capacitor or inductor degradation
Electrical sensors [15]	Open circuit Wear-out (tuning parameter drift)

characteristic outputs precisely in real-time [26]. To the best of our knowledge, the digital twin concept is relatively new for power electronic systems and has not yet been applied for fault diagnosis in a distributed PV system.

We present the design, development, and experimental validation of a digital twin approach for fault diagnosis in a distributed power electronic-based PV system. The proposed approach performs fault diagnosis of each individual PVECU and enhances the dependability of the overall PV system. A model-based digital twin is developed for each PVECU. An error residual vector is generated by comparing the outputs of the digital twin with the outputs of the physical twin. Analytic evaluation of the error residual vector enables to FD and FI.

The proposed approach operates by leveraging the sensing, processing, and actuation capabilities of the distributed power electronic converters (i.e. the panel-level power converters in these systems). Thus, such an approach obviates the need for extra hardware resources and relaxes the communication requirements which enable better performance than the state-of-the-art approaches.

The proposed fault diagnosis approach is validated in realistic outdoor field conditions. A 300 W panel-level power converter prototype is designed, developed, and tested to perform outdoor field experiments. Next, a PVECU is deployed on a building rooftop to demonstrate the proposed approach. The experimental results show the effectiveness of the proposed approach in detecting and identifying ten different faults in the PVECU which no other existing approach achieves. These ten faults are grouped into three categories: 1) PV panel faults, 2) panel-level power converter faults, and 3) electrical sensor faults. A central feature of the proposed approach is its ability to detect faults in the input energy source (i.e. the PV panel in this work) and distinguish them from the power converter and sensor faults. Moreover, the time to FD and FI is comparable to those of existing approaches. This work also demonstrates higher sensitivity to incipient PVECU faults (e.g. faults in an electrical sensor) than that of existing approaches.

The remainder of the paper is organized as follows. Section II presents an overview of a distributed power electronic-based PV system. Section III develops the modeling framework for the digital twin estimator. Section IV presents the digital twin approach for fault diagnosis, which includes both FD and FI methodologies. Section V presents the implementation details and hardware setup for the field experiments. The experimental results and related analysis that validate the digital twin approach for fault diagnosis are presented in Section VI. Section VII concludes the paper.

II. AN OVERVIEW OF THE DISTRIBUTED POWER ELECTRONIC-BASED PV SYSTEM

In this section, an overview of the distributed power electronic-based PV system is presented to illustrate the concepts put forward. Fig. 1 shows a candidate dc-based power conversion architecture using the PVECU concept. The panel-level power converter of each PVECU performs maximum power point tracking (MPPT). The PVECUs are connected in series to form a PV string which is connected to a 380 Vdc distribution bus. It is assumed that the bus voltage is maintained constant by another entity (e.g. a battery bank) in the distribution network and each PV string operates as a current source. Moreover, in this study, it is assumed that there are always sufficient loads in the system to sink the available PV power.

Fig. 2 shows the schematic of a PVECU power stage including a four-switch buck-boost converter circuit topology. The buck-boost converter is chosen because it can operate in three modes: buck, boost, and bridge, which provides design flexibility for the distributed PV system architecture and size [3]. Moreover, the authors in [8] evaluate various types of dc-dc converter topologies for the series-connected PVECUs and conclude that the four-switch buck-boost converter provides the greatest flexibility in placing any number of PV panels in a string and has an optimal efficiency-density Pareto front. The authors in [3], [8], [27] present additional advantages of the four-switch buck-boost converter in distributed PV systems including higher efficiency and reliability than those of the two-switch buck-boost converter.

Fig. 1 shows the PVECU control & monitoring stage which hosts the fault diagnosis and control on a single computing platform. It also presents the operational elements which perform fault diagnosis of each PVECU locally. The three main elements of the fault diagnosis approach are: 1) a digital twin which estimates the measurable characteristic outputs $\mathbf{z}(t)$ of the PVECU in real-time; 2) an error residual vector $\boldsymbol{\gamma}(t)$ which is the difference between the estimated outputs $\mathbf{z}(t)$ and the measured outputs $\mathbf{y}(t)$, and a FD methodology which triggers FD flag; and 3) analytic evaluation of the error residual vector $\boldsymbol{\gamma}(t)$ to precisely identify the faulted subcomponent and its failure mechanism (indicated by FI flag). Note that the fault signature library includes a priori knowledge about the possible fault events and is an ensemble of analytically computed n fault signatures $\mathbf{f}_i \; \forall \; i \in \{1, 2, ..., n\}$. These three elements are described in detail in the subsequent sections.

III. DIGITAL TWIN ESTIMATOR

A digital twin estimator is the first element of the fault diagnosis approach as shown in Fig. 1. It is a digital emulation of a physical system that analytically computes the measurable characteristic outputs in real-time [26]. It could
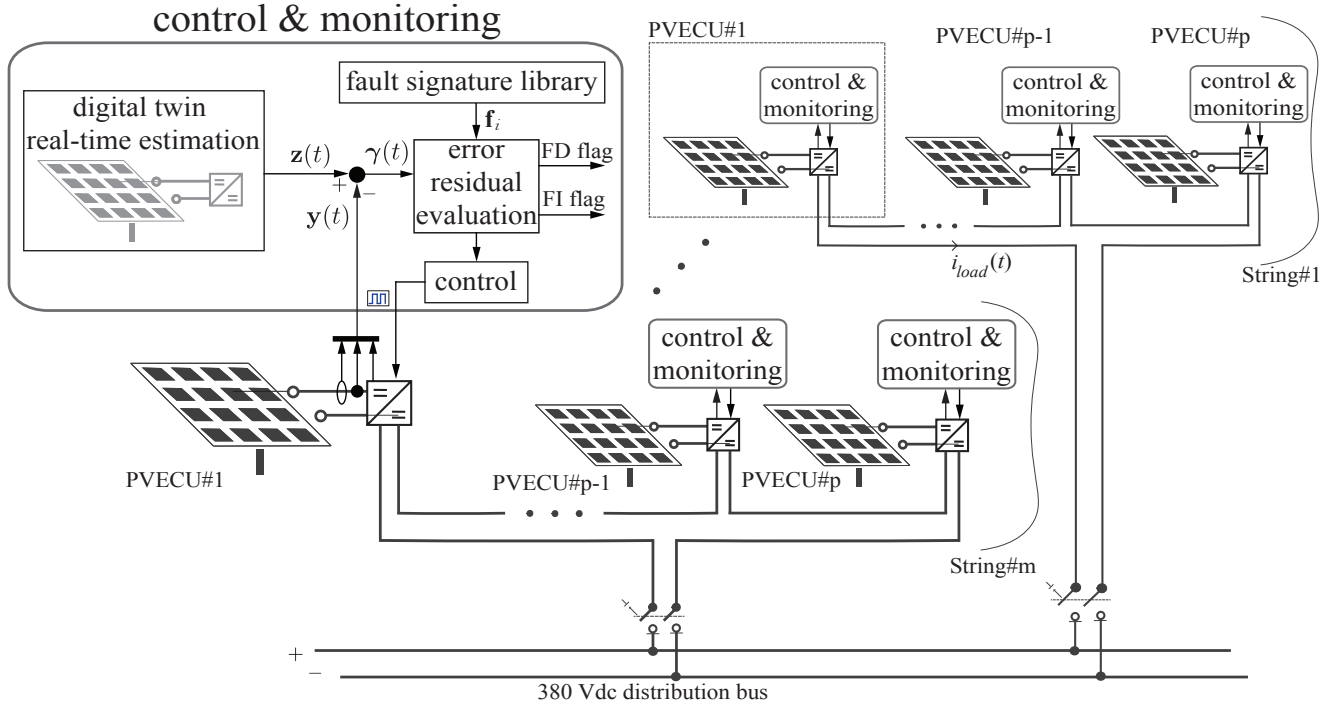
Fig. 1: A candidate distributed power electronic-based PV system for building applications. An overview of a digital twin approach for fault diagnosis of the complete PV system is also shown. p is the number of PVECUs in a string. m is the number of strings.
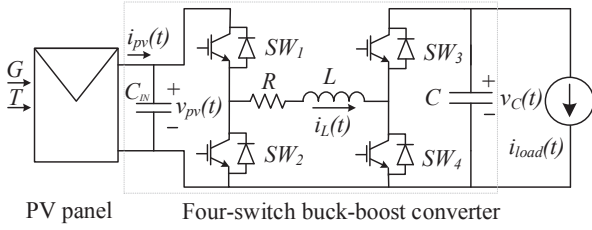

Fig. 2: Schematic of a PVECU power stage.

be model-based or data-driven or a combination of both. The following set of equations present the model-based digital twin estimator of a PVECU which has an arbitrary power electronic converter:

$$
\begin{aligned}
\mathbf{z}[k, G, T] &= \mathbf{C} \begin{bmatrix} \mathbf{x}[k] \\ I_{pv}[G, T] \\ V_{pv}[G, T] \end{bmatrix} \\
&= \begin{bmatrix} \mathbf{x}[k] \ni \mathbf{x}[k+1] = \hat{\mathbf{A}}_j \mathbf{x}[k] + \hat{\mathbf{B}}_j \mathbf{u}[k] \\ \dfrac{I_{pv}^{ref} G\left(1 + K_i(T - T^{ref})\right)}{G^{ref}} \\ \dfrac{V_{pv}^{ref}\left(1 + K_p(T - T^{ref})\right)}{1 + K_i(T - T^{ref})} \end{bmatrix},
\end{aligned}
$$
$$
\mathbf{C} = \mathbf{I}_{s_n \times s_n}, \quad k \in \mathbb{Z} \tag{1}
$$

where $\mathbf{z}[k, G, T] \equiv \mathbf{z}(kT_s, G, T)$ is the estimated characteristic output vector in discrete-time with a sampling period of T_s; $\mathbf{x}[k]$ is the estimated power converter states; $I_{pv}[G, T]$ is the estimated PV panel operating current at maximum power point (MPP) and is a function of solar irradiance G and panel

temperature T; $V_{pv}[G, T]$ is the estimated panel operating voltage at MPP and is a function of G and T; and $\mathbf{C}$ is an identity matrix representing s_n sensor gains (s_n represents identity matrix dimension).

Next, each equation in the digital twin estimator is discussed in detail. The first element of $\mathbf{z}[k, G, T]$ represents the forward Euler-based discretization of the linear-switched state space equation (i.e. $\dot{\mathbf{x}}(t) = \mathbf{A}_{\sigma(t)}\mathbf{x}(t) + \mathbf{B}_{\sigma(t)}\mathbf{u}(t)$ [15]) with a sampling period of T_s for an arbitrary power converter with piece-wise linear elements [28]. Thus, when $t = kT_s$ where $k \in \mathbb{Z}$, $\mathbf{x}(kT_s) \equiv \mathbf{x}[k]$ is the state vector; $\mathbf{u}(kT_s) \equiv \mathbf{u}[k]$ is the input vector; and the continuous-time switching function $\sigma(t)$ maps the time into an index set $\{1, 2, ..., nm\}$. Each of the indices indicates a particular model of the system given by the doublets $(\mathcal{A}_j, \mathcal{B}_j)$ where $j \in \{1, 2, ..., nm\}$. That is, $\mathbf{A}_{\sigma(t)} \in \mathcal{A} \triangleq \{\mathcal{A}_1, \mathcal{A}_2, ..., \mathcal{A}_{nm}\}$ and $\mathbf{B}_{\sigma(t)} \in \mathcal{B} \triangleq \{\mathcal{B}_1, \mathcal{B}_2, ..., \mathcal{B}_{nm}\}$. Thus, in $\mathbf{x}[k+1] = \hat{\mathbf{A}}_j \mathbf{x}[k] + \hat{\mathbf{B}}_j \mathbf{u}[k]$, $\hat{\mathbf{A}}_j = \mathbf{I} + T_s \mathbf{A}_{\sigma(t)}$ and $\hat{\mathbf{B}}_j = T_s \mathbf{B}_{\sigma(t)}$.

The second element of $\mathbf{z}[k, G, T]$ represents the operating current of the PV panel which corresponds to its MPP for a given G and T. Equation (2) models the panel operating current [29]:

$$
I_{pv}[G, T] = \frac{I_{pv}^{ref} G\left(1 + K_i(T - T^{ref})\right)}{G^{ref}} \tag{2}
$$

where $I_{pv}[G, T]$ is the operational panel current at MPP when the incident solar irradiance is G and the panel temperature is T; I_{pv}^{ref} is the operating current at MPP at the reference solar irradiance G^{ref} and temperature T^{ref}; and K_i is the current temperature coefficient.

The last element of $\mathbf{z}[k, G, T]$ models the operating
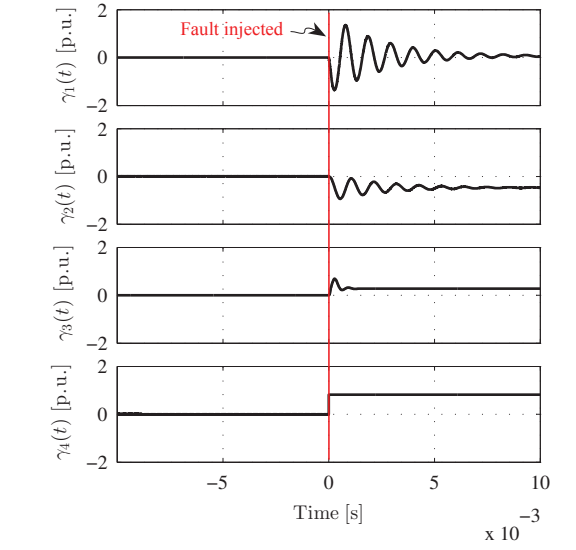
(a) Error residual $\boldsymbol{\gamma}(t)$ before and after a fault event in a PVECU.
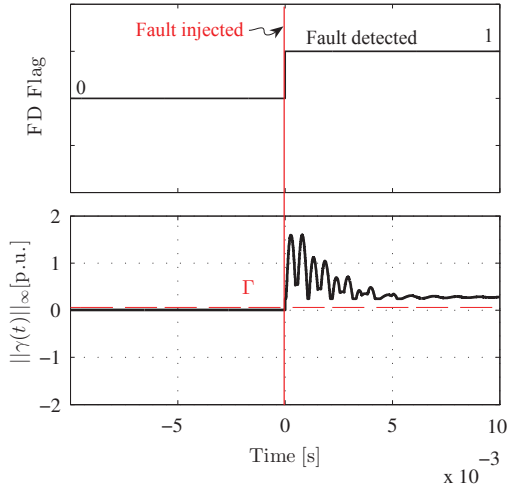
(b) FD logic. FD Flag indicating fault event (top). Comparison of the infinity norm of $\boldsymbol{\gamma}(t)$ and the threshold value Γ (bottom).

Fig. 3: Simulation results for the FD methodology.

voltage of the PV panel which corresponds to its MPP through (3) [30]:

$$
\begin{aligned}
V_{pv}[G,T] &= \frac{P_{pv}[G,T]}{I_{pv}[G,T]} = \frac{P_{pv}^{ref}\dfrac{G}{G^{ref}}\left(1 + K_p(T - T^{ref})\right)}{I_{pv}[G,T]} \\
&= \frac{V_{pv}^{ref}\left(1 + K_p(T - T^{ref})\right)}{1 + K_i(T - T^{ref})}
\end{aligned} \tag{3}
$$

where $V_{pv}[G,T]$ is the operational panel voltage at MPP for a given G and T; P_{pv}^{ref} is the maximum panel power at G^{ref} and T^{ref}; V_{pv}^{ref} is the operating voltage at P_{pv}^{ref}; and K_p is the maximum panel power temperature coefficient.

Equations (2) and (3) approximate the panel current and voltage at MPP. These estimated values are compared with the measured values of a PV panel under regulated G and T conditions to calculate estimation errors for the digital twin estimator. The estimation errors for both equations are within

$\pm 5\%$ for the operating range of G and T (see Appendix A). Note that field applications of these equations require a basic weather station to communicate the real-time information of solar irradiance and panel temperature.

This work presents a model-based digital twin estimator of a PVECU which has a four-switch buck-boost converter as shown in Fig. 2. The estimated outputs $\mathbf{z}(t)$ (in the continuous-time) of the PVECU digital twin include power converter inductor current $\hat{i}_L(t)$, power converter capacitor voltage $\hat{v}_C(t)$, PV panel MPP current $I_{pv}(G,T)$, and PV panel MPP voltage $V_{pv}(G,T)$. Note that in a fault-free (healthy) case, outputs of the digital twin are nominally the same as that of the physical twin irrespective of input conditions (G, T, and $i_{load}(t)$). Thus, the digital twin estimator for the PVECU in Fig. 2 (where $t = kT_s$) is:

$$
\mathbf{z}[k, G, T] = \mathbf{C}\begin{bmatrix}\mathbf{x}[k] \\ I_{pv}[G,T] \\ V_{pv}[G,T]\end{bmatrix}, \mathbf{x}[k] = \begin{bmatrix}\hat{i}_L[k] \\ \hat{v}_C[k]\end{bmatrix},
$$

$$
\mathbf{u}[k] = \begin{bmatrix}v_{pv}[k] \\ i_{load}[k]\end{bmatrix}, \hat{\mathbf{A}}_j = \mathbf{I}_{2\times 2} + T_s\begin{bmatrix}-\dfrac{R}{L} & -\dfrac{s_3}{L} \\ \dfrac{s_3}{C} & 0\end{bmatrix},
$$

$$
\hat{\mathbf{B}}_j = T_s\begin{bmatrix}\dfrac{s_1}{L} & 0 \\ 0 & -\dfrac{1}{C}\end{bmatrix}, \mathbf{C} = \mathbf{I}_{4\times 4},
$$

$$
j \in \{1,2,3,4\}, \ s_1 \in \{0,1\}, \ s_3 \in \{0,1\}
$$

The reference values, I_{pv}^{ref} and V_{pv}^{ref} in (2) and (3) are chosen as the MPP current (I_{MPP}) and voltage (V_{MPP}) at standard test condition (i.e. $G^{ref} = 1000$ W/m^2 and $T^{ref} = 25°$C) which are generally available in a PV panel datasheet.

IV. Fault Diagnosis via Digital Twin

In this section, the FD and FI methodologies based on the digital twin estimator are illustrated with simulation results to describe their working principles and operation. Lastly, simulation results for the fault diagnosis of a representative distributed PV system are presented to demonstrate the operation of the proposed approach in a system setting.

A. FD Methodology

The generation of $\boldsymbol{\gamma}(t)$ for FD is the second element of the fault diagnosis approach as shown in Fig. 1. Note that (4) and (5) are also implemented digitally, but are presented in the continuous-time domain. The measured system outputs $\mathbf{y}(t)$ are subtracted from the estimated outputs $\mathbf{z}(t)$ to generate $\boldsymbol{\gamma}(t)$ as given in (4):

$$
\boldsymbol{\gamma}(t) = \mathbf{z}(t) - \mathbf{y}(t) = \begin{bmatrix}\gamma_1(t) \\ \gamma_2(t) \\ \gamma_3(t) \\ \gamma_4(t)\end{bmatrix} = \begin{bmatrix}\hat{i}_L(t) - i_L(t) \\ \hat{v}_C(t) - v_C(t) \\ I_{pv}(G,T) - i_{pv}(t) \\ V_{pv}(G,T) - v_{pv}(t)\end{bmatrix} \tag{4}
$$

To scale the heterogeneous elements of $\boldsymbol{\gamma}(t)$ to a common range, $\boldsymbol{\gamma}(t)$ is converted into per unit (p.u.) values. The L^∞ norm $||\boldsymbol{\gamma}(t)||_\infty$ can be easily computed and is used to detect a fault event. In the fault-free scenario, the norm is arbitrarily close to zero, with deviations arising due to analytical estimation errors, discretization errors, and system noises (e.g. due to sensors). To counteract these deviations and

TABLE II
PV ENERGY CONVERSION SYSTEM SPECIFICATIONS

PV panel ratings	260 W, 8.95 A (I_{sc}), 37.7 V (V_{oc}), 8.58 A (I_{MPP}), 30.3 V (V_{MPP}) [CSUN 260-60P]
Controlled dc load	Resistor banks
Buck-Boost converter ratings	300 W, 100 V, 20 A [Table III]
Solar irradiance sensor	Pyranometer, Basis SMP11-A (4-20 mA) [KIPP & ZONEN]
Panel Temperature sensor	PT-100

to minimize false alarm rates in FD, the threshold value Γ is chosen by the following procedure:

1) the upper bound is computed for each element of the fault-free $\boldsymbol{\gamma}(t)$ (i.e. $\gamma_l(t) \ \forall \ l \in \{1, 2, 3, 4\}$) such that $|\gamma_l(t)| \leq |\epsilon_l| + |n| + |d_e|$ where ϵ_l represents the estimation error in each element (see Appendix A), n is the noise determined from the experimental tests, and d_e is the error due to discretization and quantization deduced after the digital implementation.

2) the L^∞ norm $||\boldsymbol{\gamma}(t)||_\infty$ is calculated and a safety margin m_S is added to achieve tolerance against a maximum level of noise in the experimental conditions. Thus $\Gamma = ||\boldsymbol{\gamma}(t)||_\infty + |m_S|$.

A FD flag indicates the fault event according to the following logic:

$$||\boldsymbol{\gamma}(t)||_\infty \geq \Gamma, \ \text{FD flag} = 1$$
$$||\boldsymbol{\gamma}(t)||_\infty < \Gamma, \ \text{FD flag} = 0 \tag{5}$$

The PVECU and its digital twin estimator are simulated in MATLAB/Simulink using the Piecewise Linear Electrical Circuit Simulation (PLECS) toolbox. The simulation parameters are given in Table II. Fig. 3a shows $\boldsymbol{\gamma}(t)$ before and after a fault event. As shown, $\boldsymbol{\gamma}(t)$ is arbitrarily close to zero before the fault is injected. However, after the fault event, it evolves in time depending on the fault type. Fig. 3b shows the FD logic which compares $||\boldsymbol{\gamma}(t)||_\infty$ with $\Gamma = 0.2$. As shown, the fault is detected in one simulation time step after the fault is injected.

B. FI Methodology

Error residual evaluation for FI is the third element of the fault diagnosis approach as shown in Fig. 1. Note that the fault signatures and (9) are also implemented digitally, but are presented in the continuous-time domain. The FI methodology is broken into three parts as follows:

1) Residual Analysis for Fault Signatures: After a fault event, the dynamics of $\boldsymbol{\gamma}(t)$ evolve and take a unique direction in the fault space indicating the fault type. To determine the direction in the fault space, the error residual $\boldsymbol{\gamma}(t)$ is normalized to a unity vector $\mathbf{f}$ such that $\mathbf{f} = \xi(t)\boldsymbol{\gamma}(t)$ and $\xi(t) = \frac{1}{||\boldsymbol{\gamma}(t)||_2}$. Thus, the unit vector $\mathbf{f}$ represents the unique direction of the fault event and the L^2 norm $||\boldsymbol{\gamma}(t)||_2$ represents the fault magnitude (that is $\frac{1}{\xi(t)}$). Note that $\boldsymbol{\gamma}(t) = \frac{\mathbf{f}}{\xi(t)}$.

We analytically calculate $\boldsymbol{\gamma}(t)$ for every fault of interest in the system and validate the calculated $\boldsymbol{\gamma}(t)$ through simulation and experimental tests. The error residual vectors are then transformed into fault signatures through normalization and assembled into a *fault signature library*.

TABLE III
BUCK-BOOST CONVERTER SPECIFICATIONS

Input Voltage Range	15 V...50 V
Output Voltage Range	15 V...100 V
Max Output Power	300 W
Max Input Current	10 A
Max Output Current	20 A
Power components	
Input MOSFETS[1]	80 V, 1.9 mΩ, 180 A
Output MOSFETS[2]	150 V, 6.5 mΩ, 130 A
L	150 μH
R	80 mΩ
C	300 μF, 200 V
C_{IN}	1.6 mF, 63 V
Components for control & monitoring	
Computing device	Artix-35T FPGA
Device time step	500 ns
Switching Frequency	50 kHz
Voltage sensor bandwidth	500 kHz
Current sensor bandwidth	500 kHz

[1] [IPB019N08N3]
[2] [IPB065N15N3]

2) Fault Signature Calculation: Fault signatures are calculated analytically for sixteen types of faults which are grouped into three categories: 1) PV panel faults, 2) power converter faults, and 3) electrical sensor faults. The probabilities of the occurrence of these faults in a PVECU network depend upon operating conditions and the system specification and architecture.

PVECU faults are modeled on the digital twin estimator to analytically obtain their respective fault signatures. Thus, for a fault event in a physical system, a faulted digital twin is the one which estimates the outputs of the faulted physical system. For $\boldsymbol{\gamma}(t)$ generation in (4), the steady state outputs of a faulted digital twin are subtracted from those of a fault-free (healthy) digital twin. Note that the fault-free digital twin estimator in steady state is given by:

$$\mathbf{z}(t) = \mathbf{C} \begin{bmatrix} \frac{i_{load}(t)}{D_{s_3}}, & -\frac{R*i_{load}(t)-D_{s_1}*D_{s_3}*v_{pv}(t)}{D_{s_3}^2}, \\ \frac{I_{pv}^{ref} G\left(1+K_i(T-T^{ref})\right)}{G^{ref}}, \\ \frac{V_{pv}^{ref}\left(1+K_p(T-T^{ref})\right)}{1+K_i(T-T^{ref})} \end{bmatrix}^T \tag{6}$$

where D_{s_3} is the duty cycle for SW_3 and D_{s_1} is the duty cycle for SW_1 (see Fig. 2). A fault signature $\mathbf{f}_i$ is extracted through the analysis of $\boldsymbol{\gamma}(t)$ as presented in Section IV-B1. Table VI in Appendix B presents $\mathbf{f}_i$ and $\frac{1}{\xi(t)}$ for all $i \in \{1, 2, ..., 16\}$.

The fault signature calculation is illustrated for a PV panel fault type $i = 1$. Consider the soiling of the PV panel. It causes the value of I_{pv}^{ref} for the faulted panel to change by a quantity ΔI_{pv}^{ref} for G^{ref} (note that the change in V_{pv}^{ref} is negligible). Thus, the faulted digital twin estimator in steady state is given

by:

$$\tilde{\mathbf{z}}(t) = \mathbf{C} \begin{bmatrix} \frac{i_{load}(t)}{D_{s_3}}, & -\frac{R*i_{load}(t)-D_{s_1}*D_{s_3}*v_{pv}(t)}{D_{s_3}^2}, \\ \frac{(I_{pv}^{ref}-\Delta I_{pv}^{ref})G(1+K_i(T-T^{ref}))}{G^{ref}}, \\ \frac{V_{pv}^{ref}(1+K_p(T-T^{ref}))}{1+K_i(T-T^{ref})} \end{bmatrix}^T \quad (7)$$

In this case, the error residual vector $\boldsymbol{\gamma}(t) = \mathbf{z}(t) - \tilde{\mathbf{z}}(t)$ is $\mathbf{C}\left[0, 0, \frac{\Delta I_{pv}^{ref}G(1+K_i(T-T^{ref}))}{G^{ref}}, 0\right]^T$. For its normalization, it is divided by $||\boldsymbol{\gamma}(t)||_2$ which represents the fault magnitude $\frac{1}{\xi(t)}$ and is $\frac{\Delta I_{pv}^{ref}G(1+K_i(T-T^{ref}))}{G^{ref}}$. This normalization results in a unity vector $\mathbf{f_1}$ which is the fault signature and is $[0, 0, 1, 0]^T$.

For power converter faults, the signature calculation for fault type $i = 4$ is illustrated. Consider an open switch fault in SW_1 in Fig. 2. The fault event causes the open circuit of the PV panel. Thus, the faulted digital twin estimator in steady state is $\tilde{\mathbf{z}}(t) = \mathbf{C}\begin{bmatrix} 0, 0, 0, V_{oc} \end{bmatrix}^T$. The error residual $\boldsymbol{\gamma}(t)$ is generated and analyzed to obtain $\mathbf{f_4}$ and $\frac{1}{\xi(t)}$ which are given in Table VI in Appendix B.

For electrical sensor faults, the signature calculation for fault type $i = 12$ is illustrated. Consider a $\Delta c_{12}(t)$ drift and a $\Delta e_{12}(t)$ offset in $i_L(t)$ sensor. This sensor fault can be modeled in the measured physical system outputs as (see [15]):

$$\mathbf{y}(t) = (\mathbf{C} + \Delta\mathbf{C}(t)) \begin{bmatrix} i_L(t) \\ v_C(t) \\ i_{pv}(t) \\ v_{pv}(t) \end{bmatrix} + \Delta\mathbf{E}(t),$$

$$\Delta\mathbf{C}(t) = \begin{bmatrix} \Delta c_{12}(t) & 0 \\ 0 & \mathbf{0}_{3\times3} \end{bmatrix}, \quad \Delta\mathbf{E}(t) = \begin{bmatrix} \Delta e_{12}(t) \\ 0 \\ 0 \\ 0 \end{bmatrix} \quad (8)$$

In this case, the error residual $\boldsymbol{\gamma}(t) = \mathbf{z}(t) - \mathbf{y}(t)$ is $[\Delta c_{12}(t)i_L(t) + \Delta e_{12}(t), 0, 0, 0]^T$. Thus, $\mathbf{f_{12}} = [1, 0, 0, 0]^T$ and $\frac{1}{\xi(t)} = \Delta c_{12}(t)i_L(t) + \Delta e_{12}(t)$. Note that $\mathbf{z}(t) = \mathbf{C}[\hat{i}_L(t), \hat{v}_C(t), I_{pv}(G, T), V_{pv}(G, T)]$ is nominally the same as $\mathbf{y}(t) = \mathbf{C}[i_L(t), v_C(t), i_{pv}(t), v_{pv}(t)]$ in a fault-free case.

Similarly, one can compute the fault signatures for other PVECU fault types listed in Table VI.

3) FI Logic: After a fault event, $\boldsymbol{\gamma}(t)$ takes a unique direction in the fault space that indicates the fault type. Thus after FD, an L^2 inner product is computed between $\boldsymbol{\gamma}(t)$ and every member of the fault signature library (i.e. $\{\mathbf{f_1}, \cdots, \mathbf{f_{16}}\}$) in real-time. It reveals the projection of $\boldsymbol{\gamma}(t)$ on each $\mathbf{f}_i$. Intuitively, the maximum magnitude of inner product will be between $\boldsymbol{\gamma}(t)$ and the $\mathbf{f}_i$ with which it most closely aligns to. The maximum inner product search indicates the fault type i identifying the fault event. Thus, a FI logic computes the inner products and performs the maximum inner product search.
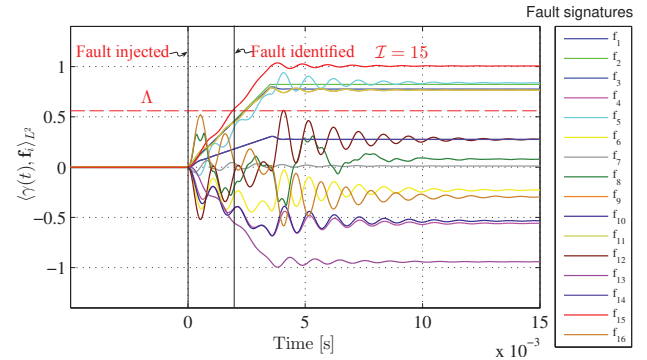
The L^2 inner product is mathematically obtained as follows: $\langle\boldsymbol{\gamma}(t), \mathbf{f}_i\rangle_{L^2} = \int_{t-W}^{t} \boldsymbol{\gamma}^T(t-\tau)\mathbf{f}_i(\tau)\,\mathrm{d}\tau$ where W represents the window size over which the inner product is calculated. Thus, for a given fault signature library $\{\mathbf{f_1}, \cdots, \mathbf{f_{16}}\}$ (see Appendix B), the FI logic computes
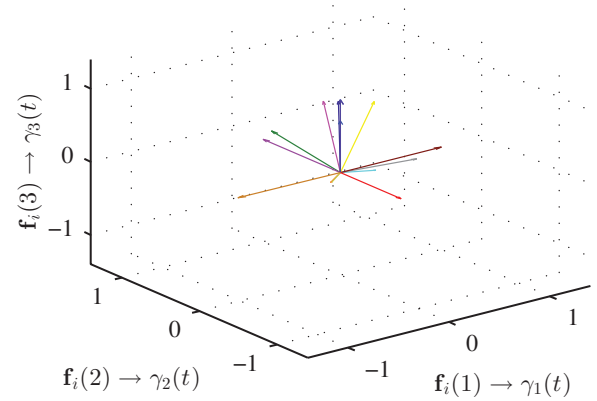
(a) First three elements of the sixteen fault signatures.
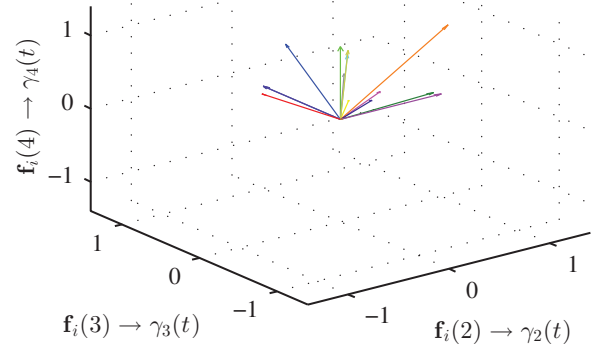
(b) Last three elements of the sixteen fault signatures.

(c) Inner products between $\boldsymbol{\gamma}(t)$ and fault signature library to identify fault type.

Fig. 4: Simulation results for the FI methodology. Graphical representation of the fault signature library, where each fault signature $\mathbf{f}_i = \xi(t)[\gamma_1(t), \gamma_2(t), \gamma_3(t), \gamma_4(t)]^T \ \forall \ i \in \{1, \cdots, 16\}$ shows a unique direction in the fault space (top). FI logic (bottom).

$$\mathcal{I} = \begin{cases} i & \text{if } \max\limits_{i\in\{1,\cdots,16\}} \langle\boldsymbol{\gamma}(t), \mathbf{f}_i\rangle_{L^2} \geq \Lambda \\ 0 & \text{if } \max\limits_{i\in\{1,\cdots,16\}} \langle\boldsymbol{\gamma}(t), \mathbf{f}_i\rangle_{L^2} < \Lambda \end{cases} \quad (9)$$

where $\mathcal{I}$ indicates the fault type through the FI flag and Λ is the empirically calculated FI threshold to minimize the false identification of fault type during the transient.

Fig. 4 presents the simulation results for the FI methodology. The graphical representations of the fault signa-
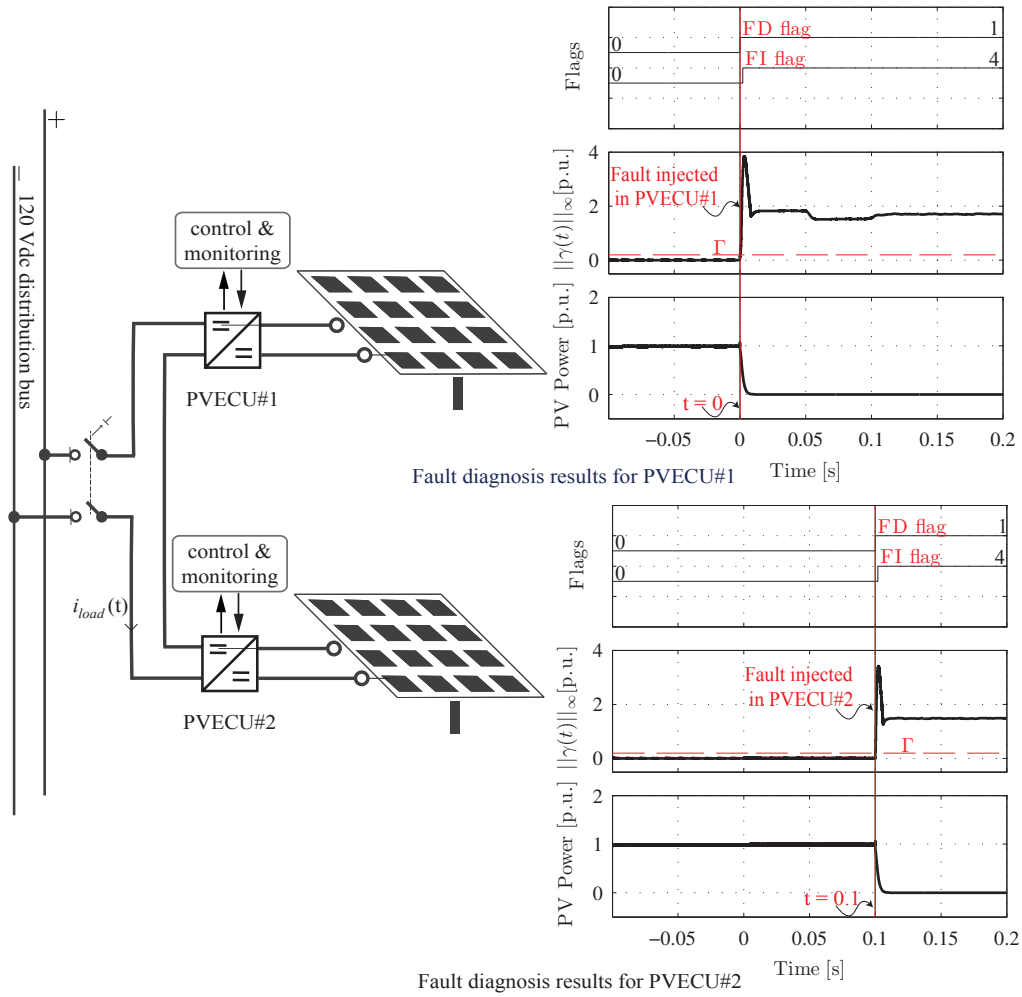
Fig. 5: Simulation results for fault diagnosis in a representative distributed PV system. Diagnosis of a fault injected at $t = 0$ [$t = 0.1$] in PVECU#1 [PVECU#2] is shown in the top [bottom] subfigure.

ture library show the direction taken by each $\mathbf{f}_i$ (a $\mathbf{f}_i = \xi(t)[\gamma_1(t), \gamma_2(t), \gamma_3(t), \gamma_4(t)]^T$). Fig. 4a presents the direction when the $\mathbf{f}_i$ has $\mathbf{f}_i(1), \mathbf{f}_i(2)$, and $\mathbf{f}_i(3)$ for all $i \in \{1, 2, ..., 16\}$. Fig. 4b presents the direction with the last three elements (i.e. $\mathbf{f}_i(2), \mathbf{f}_i(3)$, and $\mathbf{f}_i(4)$). Fig. 4c presents the FI logic which activates after FD. The logic identifies the fault event which is detected in Fig. 3b. It shows the evolution of the sixteen inner products performed between $\boldsymbol{\gamma}(t)$ and each $\mathbf{f}_i$ over a window size of 2 ms. These inner products are compared with $\Lambda = 0.6$ to prevent the initial false identification of fault type when $\boldsymbol{\gamma}(t)$ is still evolving in the fault space (during the transient). Fault type $\mathcal{I} = 15$ (see Table VI) is identified within 2 ms when the maximum inner product (out of all sixteen) exceeds the Λ.

C. Simulation Study for a Distributed PV System

To show the operation of the proposed fault diagnosis approach in a system setting, a simulation study is performed on a representative distributed PV system which is shown in Fig. 5. The system consists of a two series-connected PVECUs (i.e. PVECU#1 and PVECU#2) forming a string which is connected to a 120 V dc distribution bus (since only

2 PVECUs are considered). As shown in Fig. 5, both PVECUs have their own control & monitoring (which include the proposed fault diagnosis) stages. The simulation parameters for a PVECU are given in Table II and III. The simulation results for the fault diagnosis of each PVECU are presented adjacent to its schematic in Fig. 5. An open switch fault in SW_1 (see Fig. 2) is injected in PVECU#1 at $t = 0$ (see top subfigure in Fig. 5) and the same fault type is injected in PVECU#2 after 0.1s (see bottom subfigure in Fig. 5). As shown, after fault injection in the PVECU, the corresponding PV panel power goes to 0. This fault event causes $||\boldsymbol{\gamma}(t)||_\infty$ to become non-zero in each PVECU after the time of fault injection and triggers the FD and FI flags.

In PVECU#1, $||\boldsymbol{\gamma}(t)||_\infty$ exceeds the threshold and triggers the FD flag after one simulation time step (see top subfigure in Fig. 5). After FD, the FI function is activated that identifies the fault type as $i = 4$. Note that the FD and FI flags for PVECU#2 do not change during the fault event in PVECU#1. Later at $t = 0.1$, the open switch fault is injected in PVECU#2 which is also detected and identified correctly as shown in the bottom subfigure of Fig. 5. The fault event in PVECU#2

(a) Four-switch buck-boost converter prototype

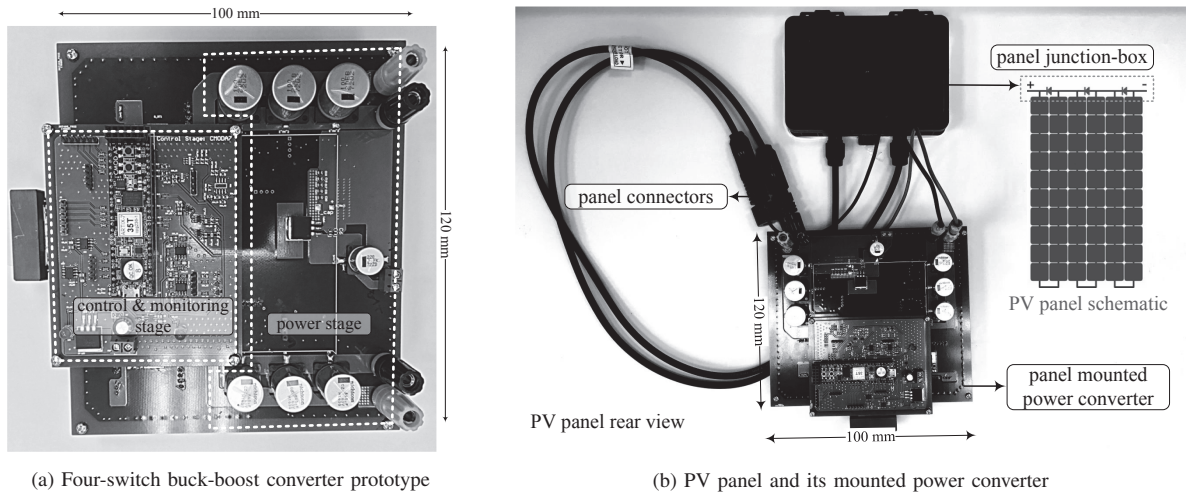(b) PV panel and its mounted power converter

Fig. 6: Annotated photographs presenting panel-level power converter and its mounting details on a PV panel for conducting outdoor field experiments.

does not alter the FD and FI flags of PVECU#1. Similarly, a distributed PV system with more than two PVECUs in a string or with multiple strings can also be simulated for other fault events.

V. IMPLEMENTATION DETAILS AND HARDWARE SETUP FOR FIELD EXPERIMENTS

This section presents the implementation details and hardware setup for the outdoor field experiments to validate the proposed fault diagnosis approach. Since the dynamics of the PV panel faults are slow and can be better emulated in a real settings than through a PV emulator, we choose to perform experiments in an open space located on a flat roof of a building on the National University of Singapore campus. A 10 kW PV system along with a weather station has been installed in that space for various research purposes. The following are the step-by-step details for the outdoor field experimental validation.

A. Power Converter Prototype

First, a PV panel mounted 300 W buck-boost converter prototype is designed and developed. The power stage has four silicon MOSFET switches, four isolated gate drivers, a bank of input and output capacitors, an inductor, and on-board isolated current and voltage sensing devices. The control & monitoring stage uses a Xilinx Artix-7 FPGA based computing device, ADCs, and DACs. Fig. 6a shows the annotated photograph of the buck-boost converter prototype. Table III presents the complete specifications of the prototype and lists the details of the components for power and control & monitoring stages, respectively.

Fig. 6b presents the converter mounting details on the PV panel. In residential and commercial settings, a PV panel typically has three strings. Each string consists of 20 or 24 series connected silicon solar cells and terminates into an integrated junction box. These strings are further combined in series configuration at the junction box and an anti-parallel diode is placed across each string for PV panel protection

Fig. 7: Annotated photograph of the PV energy conversion system in field.

purposes (see Fig. 6b). The converter prototype is connected across the output terminals of the panel junction box.

B. Implementation of Fault Diagnosis Approach and Control Logic

Next, the digital twin estimator, FD and FI methodologies, and control logic are implemented on the Artix-7 FPGA (i.e. XC7A35T-1CPG236C). The reasons for choosing this FPGA include its higher performance (in terms of speed and resources), lower power consumption, smaller size package and optimized cost compared to other computing devices.

The digital twin estimator (1), FD logic (5), FI logic (9), and control logic are discretized with a fixed device time step of 500 ns and implemented on the FPGA using finite state machines and pipelining. The fault signature library in Table VI is hardcoded onto the computing device. Thus, the FPGA performs the following tasks: 1) solves the digital twin estimator; 2) generates an error residual vector based on signals from the physical twin and the digital twin; 3) stores the fault signature library; and 4) triggers the FD and FI flags based on the L^∞ norm of the error residual vector and the L^2-inner product calculation. The ADCs sample the outputs of the PV panel, the power converter, and the load current at a frequency of 500 kHz for fault diagnosis and control. The solar irradiance and temperature data are sampled at a frequency of 0.1 Hz. Note that the overall digital design uses the 48%

resources of the XC7A35T and the power consumption is 0.2 W.

In addition, the control logic includes a simple perturb and observe (P&O) method for tracking MPP under operating ranges of solar irradiance and temperature. The details of control logic are given in [3].

C. PV Energy Conversion System in Outdoor Field

Lastly, we installed a PVECU for the outdoor field experiments. Fig. 7 shows the annotated photograph of the field experimental testbed, where a 260 W PV panel is chosen and the power converter prototype is mounted on its rear side. The weather station provides the solar irradiance and panel temperature data. Table II presents addition details about the PV energy conversion system.

## VI. EXPERIMENTAL RESULTS AND DISCUSSIONS

This section presents the experimental results for diagnosis of a variety of faults listed in the fault signature library (see Table VI in Appendix B) using the field experimental testbed presented in Section V. Note that the experimental results are presented for diagnosis of those faults which have unique signatures. Later, the promptness and sensitivity [12] of the proposed approach is analyzed. Lastly, the proposed approach is compared with the prior works in the literature to display its unique and innovative features.

A. Fault Diagnosis Results

The fault diagnosis results show two types of the signals: 1) measured waveforms before and after a fault event; and 2) the digital FD and FI flag. Note that the FD flag is a *1-bit* signal which could be zero or one depending on the FD logic. Similarly, the FI flag is a *4-bit* signal presented in hexadecimal format which represents the fault type depending on the FI logic. The fault type number i corresponds to the fault event in Table VI in Appendix B.

1) PV Panel Faults: Three different types of PV panel faults are injected into the testbed.

A solar cell of the panel is shaded mildly (i.e. 20%) by an opaque object. That corresponds to $i = 1$ in Table VI. Fig. 8a presents the current-voltage and power-voltage characteristics of the PV panel before and after that fault event. Note that in a PV panel with bypass diodes, the mild shading (approximately up to 35% of a solar cell) significantly changes the MPP panel current while the change in (MPP) panel voltage from old to new MPP can be neglected. Fig. 8b shows the panel current $i_{pv}(t)$, the panel voltage $v_{pv}(t)$, and the load current $i_{load}(t)$, before and after the fault event. When the L^∞ norm of the $\gamma(t)$ exceeds the FD threshold, the fault event is detected which takes 80 ms (see FD flag). Since the shading condition disturbs the MPP of the PV panel changing both the panel current and the panel voltage simultaneously at the point of fault injection, the fault is initially identified as $i = 3$. The control logic takes around 1.2 s to reach to a new MPP of the panel. The new MPP has decreased panel current and minor change in panel voltage in comparison to those of the fault-free case. Thus,
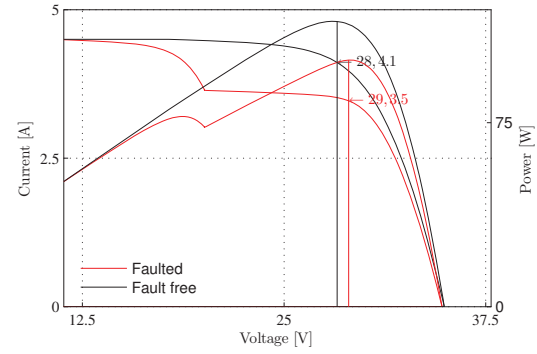
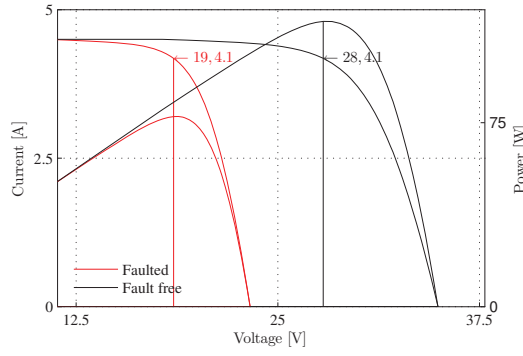(a) PV panel characteristics for faulted and fault-free conditions.
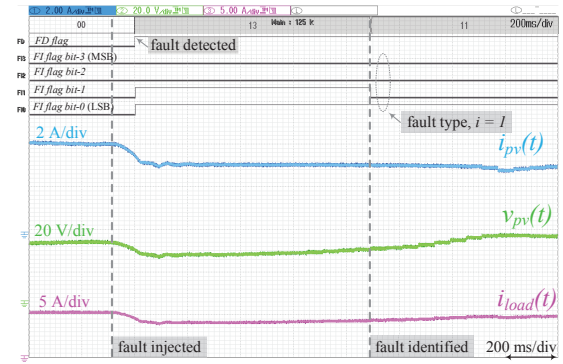
(b) Fault diagnosis.

Fig. 8: 20% shading of a solar cell in the PV panel (continuous/repetitive mild partial shading).

the fault type is identified correctly as $i = 1$, when the panel voltage is in the vicinity of the new MPP value. The time to FI is 939 ms when the inner product corresponding to $i = 1$ exceeds the FI threshold (see FI flag).

Similarly, for diagnosis of fault type $i = 2$, a solar cell of the panel is shaded severely (i.e. 40%) by an opaque object. In that scenario, one of the bypass diodes of the PV panel operates. That shifts the panel voltage to the new MPP (i.e. after severe shading) which is at the two-third of its old MPP value (i.e. fault-free) while the panel current at the new MPP remains the same as that at the old MPP. Fig. 9a presents the PV panel characteristics for fault-free and faulted (which include severe partial shading and bypass diode failures) conditions. Fig. 9b presents the panel current $i_{pv}(t)$, the panel voltage $v_{pv}(t)$, and the load current $i_{load}(t)$ before and after that fault event which is detected within 60 ms. Similar to the previous fault event, here also the initial fault type is identified as three. However, when the panel current is in the close proximity of the new MPP, the fault type is identified correctly as $i = 2$ within 1.14 s.

The fault type $i = 3$ corresponds to faults internal to the PV panel that change both its current and voltage at MPP, for instance PID of the solar cells or the interconnects. Fig. 10a presents the PV panel characteristics for $i = 3$ and fault-free conditions. We emulate PID of the PV panel by inserting a resistive element in shunt to its output terminals [31] that
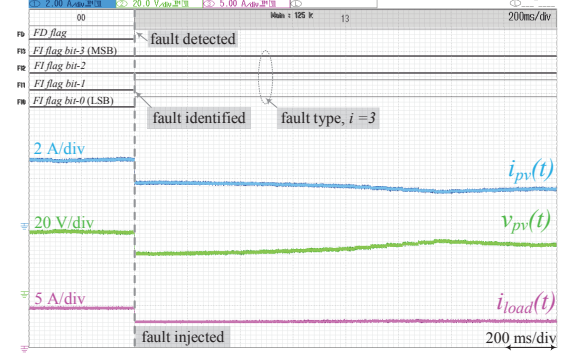
(a) PV panel characteristics for faulted and fault-free conditions.
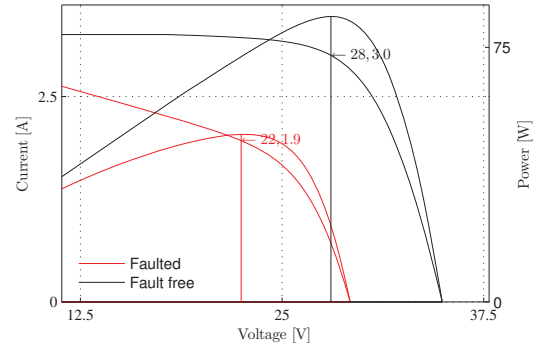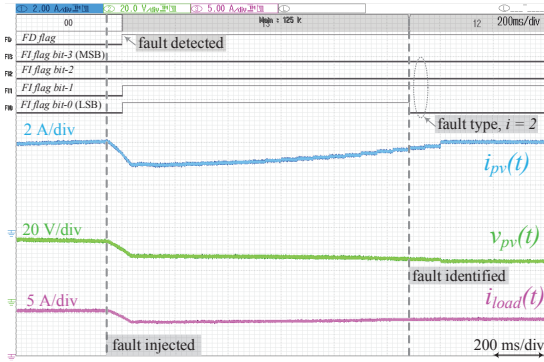
(b) Fault diagnosis.

Fig. 9: 40% shading of a solar cell in the PV panel (continuous/repetitive severe partial shading).

(a) PV panel characteristics for faulted and fault-free conditions.

(b) Fault diagnosis.

Fig. 10: Faults internal to the PV panel.

Fig. 11: Open switch fault in SW_1.

decreases the effective shunt resistance of the PV panel. Fig. 10b shows the panel current $i_{pv}(t)$, the panel voltage $v_{pv}(t)$, and the load current $i_{load}(t)$ before and after the insertion of the resistive element. The fault event is detected in 80 μs due to the instantaneous changes in the panel outputs. The fault event is identified as $i = 3$ in 2.08 ms. The control logic takes around 1.2 s to reach to a new MPP of the panel. The new MPP has both decreased, the panel current and voltage values in comparison to those of the fault-free case. Thus, in that scenario, the fault type does not change when the panel reaches the new MPP, contrary to the previous fault scenarios.

2) Power Converter Faults: The diagnosis of four types of converter switch faults (listed in Table VI) is demonstrated. Open circuit faults are injected through contactor switches and short circuit faults are injected by changing the related gating signal to one in the FPGA.

An open circuit fault in SW_1 (see Fig. 2) corresponding to $i = 4$ is injected. Fig. 11 presents the panel current $i_{pv}(t)$, the panel voltage $v_{pv}(t)$, and the inductor current $i_L(t)$ before and after the fault event. The fault event causes the open circuit of PV panel, thus the panel voltage goes to the open circuit value V_{oc}. The panel current and the inductor current go to zero. The time to FD is 14.8 μs and the fault is identified correctly as $i = 4$ within 4.01 ms. An assessment related to that performance is presented in Section VI-B.
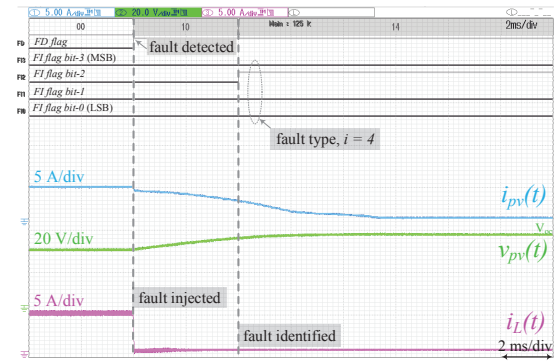
Next, a short circuit fault in SW_2 is injected. Fig. 12 shows the panel current $i_{pv}(t)$, the panel voltage $v_{pv}(t)$, and the inductor current $i_L(t)$ before and after the fault event. The fault event shorts the PV panel terminal increasing the panel current to short circuit current I_{sc}. The transient in the panel current represents the discharging current of the panel capacitor, reducing the panel terminal voltage to zero. Due to shorting of the panel output terminals, the inductor discharges its stored energy and settles to zero value. The fault event is detected very fast (i.e. 5.6 μs) and correctly identified as $i = 7$ within 2.01 ms.

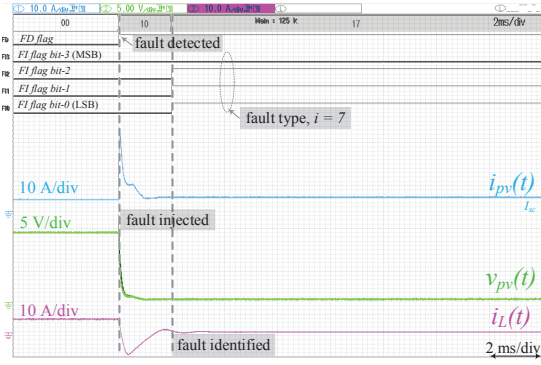Fig. 13 presents the panel current $i_{pv}(t)$, the panel voltage
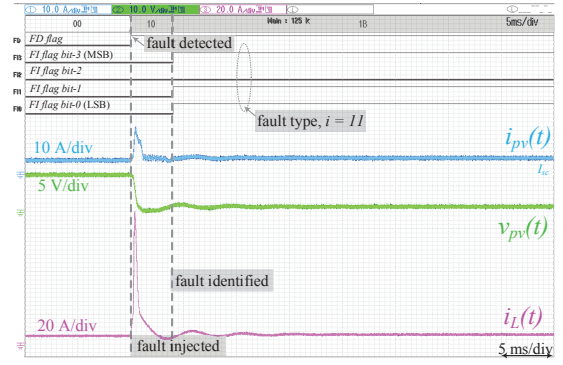
Fig. 12: Short switch fault in SW_2.

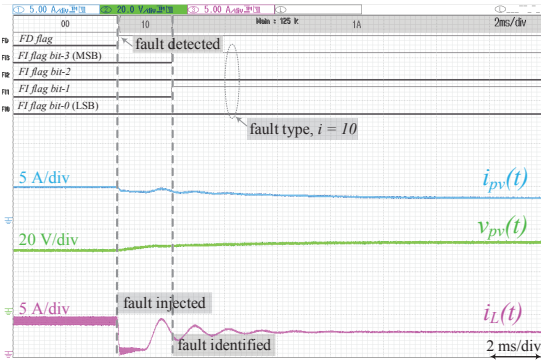Fig. 14: Short switch fault in SW_4.
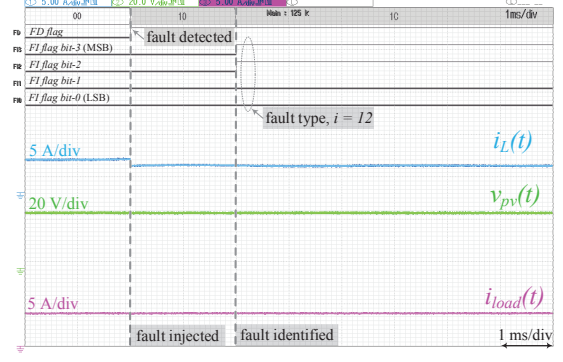

Fig. 13: Open switch fault in SW_4.

Fig. 15: 20% decrease in gain of inductor current sensor, $i_L(t)$.

$v_{pv}(t)$, and the inductor current $i_L(t)$ before and after an open fault in SW_4 is injected. The fault event can be detected and thus identified only if the power converter operates in the boost mode. That is because SW_4 is in open condition in all other modes. The open circuit in SW_4 causes the panel to work at some sub-optimal power point, thus changing the panel current and the panel voltage. The inductor discharges its pre-fault stored energy and charges to the same current value as the panel current. Time to FD is 33.6 μs and the fault event is identified as fault type $i = 10$ within 2.03 ms.

Fig. 14 shows the panel current $i_{pv}(t)$, the panel voltage $v_{pv}(t)$, and the inductor current $i_L(t)$ before and after a short fault in SW_4 is injected. The fault event shorts the PV panel through the inductor, increasing the panel current to short circuit current I_{sc}. The transient in the panel current represents the discharging current of the panel capacitance, reducing the panel terminal voltage to zero. Due to shorting of the panel output terminals through the inductor, the transient in the inductor current represents the discharging current of the input capacitance C_{IN} and its own energy. After the transient settles, the inductor current becomes equal to the panel current. The fault event is detected in 30 μs and correctly identified as fault type $i = 11$ within 4.03 ms.

3) Electrical Sensor Faults: In order to demonstrate the electrical sensor fault diagnosis, three different sensors (which include inductor current, panel output voltage, and load current

sensor, respectively) are injected with a 20% decrease in their gains in the FPGA platform. Fig. 15, 16, and 17 present the inductor current $i_L(t)$, the panel voltage $v_{pv}(t)$, and the load current $i_{load}(t)$ for diagnosis of faults in three different sensors, respectively. As shown in Fig. 15, a 20% decrease in the inductor current sensor gain causes the FD flag trigger in 1.44 μs and the FI flag shows the fault type $i = 12$ within 2.00 ms. Similarly, for a 20% decrease in the load current sensor gain shown in Fig. 16, the time to FD is 290 μs and the fault type is identified as $i = 14$ within 2.29 ms. Lastly, a decrease of 20% gain in the panel voltage sensor is detected in 1.5 μs and identified as fault type $i = 15$ within 2.00 ms as shown in Fig. 17.

B. Promptness and Sensitivity

Promptness, fault sensitivity, and robustness (i.e. immunity to false alarms) assess the performance of a fault diagnosis approach [12]. Table IV presents the promptness and sensitivity for the proposed fault diagnosis approach.

Promptness refers to the *time to FD* and the *time to FI*. The time to FD primarily relies on the dynamics of an injected fault. Faster and greater fault dynamics imply a shorter time to FD. Since PV panel faults evolve slowly due to their characteristics, the detection time is the longest. The sensor faults have the least detection time. The time to FI primarily depends upon the averaging window W over which the inner

TABLE IV
PROMPTNESS AND SENSITIVITY FOR THE PROPOSED FAULT DIAGNOSIS APPROACH

| Fault type	Fault event	Minimum fault magnitude	Time to FD	Time to FI
PV panel faults				
$i = 1$	Continuous/repetitive mild partial shading	20%	80 ms	939 ms
$i = 2$	Continuous/repetitive severe partial shading	40%	60 ms	1.14 s
$i = 3$	Internal PV panel fault (panel PID)	–	80 μs	2.08 ms
Power converter faults				
$i = 4$	Open switch fault in SW_1	–	14.8 μs	4.01 ms
$i = 7$	Short switch fault in SW_2	–	5.6 μs	2.01 ms
$i = 10$	Open switch fault in SW_4	–	33.6 μs	2.03 ms
$i = 11$	Short switch fault in SW_4	–	30 μs	4.03 ms
Electrical sensor faults				
$i = 12$	Fault in $i_L(t)$ sensor	20%	1.44 μs	2.00 ms
$i = 14$	Fault in $i_{load}(t)$ sensor	20%	290 μs	2.29 ms
$i = 15$	Fault in $v_{pv}(t)$ sensor	20%	1.5 μs	2.00 ms
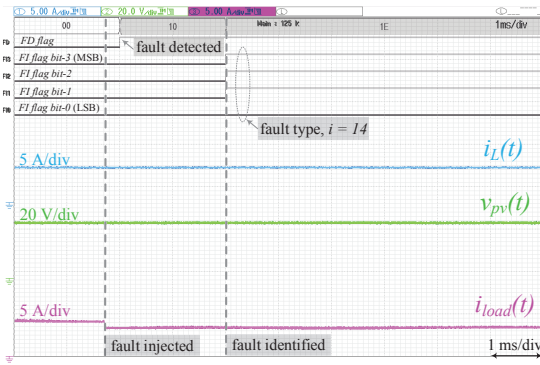
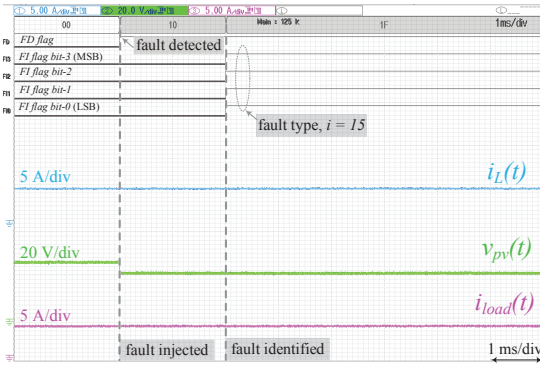Fig. 16: 20% decrease in gain of load current sensor, $i_{load}(t)$.

Fig. 17: 20% decrease in gain of PV panel voltage sensor, $v_{pv}(t)$.

product calculation is performed. Smaller window size implies a shorter time to FI. However, it also implies lesser reliability in FI. In our experiments, the size of FI window is 2 ms.

The threshold settings for FD and FI control the promptness, fault sensitivity, and robustness of the proposed approach. The choice of the FD threshold value $\Gamma = 0.2$ is the combination of the analytic and experimental study of the fault-free error residual vector as shown in Section IV-A. Similarly, FI threshold value $\Lambda = 0.6$ minimizes the false FI type.

Sensitivity refers to faults which develop slowly (i.e. incipient faults) for instance, drifts in sensor gains or hotspots due to shading conditions in a PV panel. It is quantified through

the minimum fault magnitude which causes a change in the monitored variables that can be detected by the fault diagnosis approach. Robustness refers to the immunity of a fault diagnosis approach against various noises and uncertainties reducing the number of false alarms. Note that sensitivity and robustness are two conflicting attributes. Higher sensitivity trades off the robustness of the approach. With the above mentioned choice of Γ, the proposed algorithm detects 20% drift in sensor gains and 20% mild partial shading of a solar cell in the PV panel without false alarms.

Note that PV panel faults could be intermittent or temporal or continuous. In case of intermittent and temporal PV panel faults, the system operator should look for consistency in fault flags for sufficient time before taking any fault remedial action. Fault remedial action for any other faults could be immediate.

C. Performance Comparison with Prior Works

Table V presents the performance summary of this work and the comparison with prior works in the literature. As shown in the table, most of the existing approaches are fault- and application-specific and may not be applied to other power electronic-based energy conversion systems. For instance, a fault diagnosis approach for a wind energy system is investigated in [32] and may not be applicable to a PV system. On the other side, the framework of our approach is general in principle. That is, the idea of digital twin can be ported to other energy systems (e.g. digital twin of a wind or battery energy conversion unit). The digital twin can then be used to generate residuals which are evaluated using an application-specific fault signature library (as presented in Section IV-B).

The fault signature library consists of faults of interests which are generally the common failure modes of a system (in this work - a PVECU) enabling fault-agnosticism of the proposed approach. That is, the proposed approach detects and identifies a variety of fault types, which no other existing approach achieves. The unique feature is its ability to detect faults in the input energy source and distinguish them with other types of faults related to power converter and electrical sensors. Moreover, the time to FD and FI for converter and sensor faults are comparable to the state-of-the-art. Note that the diagnosis of the PV panel faults takes a longer time due to their characteristics. This work also demonstrates the diagnosis of minimum fault magnitude for sensor and PV

TABLE V
PERFORMANCE COMPARISON OF PROPOSED FAULT DIAGNOSIS APPROACH WITH PRIOR WORKS

Work	[32]	[33]	[13]	[17]	[34]	[14]	[18]	[15]	This work
Application	wind energy systems	electrical railway traction	PV systems	PV systems	DC-DC converter systems	PV systems	PV systems	nano-grid	PV systems
Fault diagnosis approach	pole voltage estimation and error generation	state observer & residual generation	logic-based on PV panel parameters	PV panel data based	magnetic component voltage equation	shape of inductor current	online PV parameter estimation	state observer & residual generation	digital twin
Approach type	application-specific	fault-specific	application- & fault-specific	application- & fault-specific	fault-specific	fault-specific	fault-specific	general	general
Implementation platform	FPGA (quartus II)	microchip DSP	dSPACE	MatLab	DSP	FPGA	PLC	dSPACE & typhoon HIL	FPGA (Artix-7)
Power converter switching frequency	5 kHz	10 kHz	5 kHz	–	48 kHz	15 kHz	–	20 kHz	50 kHz
Fault diagnosis of energy source	no	no	no	yes	no	no	yes	no	yes
Time to FD	–	–	–	–	–	–	–	–	$\leq$ 80 ms
Time to FI	–	–	–	–	–	–	–	–	< 1.2 s
Faults diagnosis of power converters	yes, OCF & SCF	no	yes, OCF	no	yes, OCF & SCF	yes, OCF & SCF	no	yes, OCF	yes
Time to FD	< 10 μs	–	–	–	–	–	–	$\leq$ 340 μs	$\leq$ 33.6 μs
Time to FI	< 10 μs	–	$\leq$250 ms	–	< 10 μs	$\leq$ 66 μs	–	$\leq$ 113 ms	$\leq$ 4.03 ms
Fault diagnosis of sensors	no	yes	no	no	no	no	no	yes	yes
Time to FD	–	–	–	–	–	–	–	$\leq$ 360 μs	$\leq$ 290 μs
Time to FI	–	300 μs	–	–	–	–	–	$\leq$ 4.4 ms	$\leq$ 2.9 ms
Fault remediation	yes	yes	yes	no	no	yes	no	no	no
Sensitivity & robustness	no	no	no	yes	yes	no	yes	yes	yes
Threshold methodology	no	yes	–	yes	–	–	–	no	yes
Additional requirements	–	–	–	–	auxiliary winding in the magnetic core	–	auxiliary computing platform	–	G & T sensors (only for PV panel faults)

OCF = open circuit switch fault, SCF = short circuit switch fault

panel faults achieving higher sensitivity in comparison to the existing approaches. Note that fault remediation will be fault- and system architecture-specific, and is outside the scope of this paper.

VII. CONCLUSIONS

This paper presents a digital twin approach for fault diagnosis in PV installations such as rooftop and BIPV systems. These systems have decentralized and distributed power conversion architectures. The sensing, computation, and actuation capabilities of the distributed power electronics are leveraged for fault diagnosis in such systems. We design a digital twin which represents the model-based estimation of the characteristic outputs of the PV energy conversion unit in

real-time. That is followed by the error residual generation and evaluation for fault diagnosis purposes.

A source-level power converter prototype is designed and developed for validation of the fault diagnosis in the outdoor field. It hosts the proposed approach on a low-cost FPGA. The outdoor field experiments demonstrate the operation of the proposed approach in real-time and field conditions for a variety of fault types. The experimental results and their analysis show the effectiveness of the fault diagnosis approach for easy maintenance and online fault remediation, thus integrating reliability and fault tolerance.

The broad benefits of the digital twin based fault diagnosis approach for distributed power electronic-based PV systems are: 1) it can quickly detect and precisely identify a variety
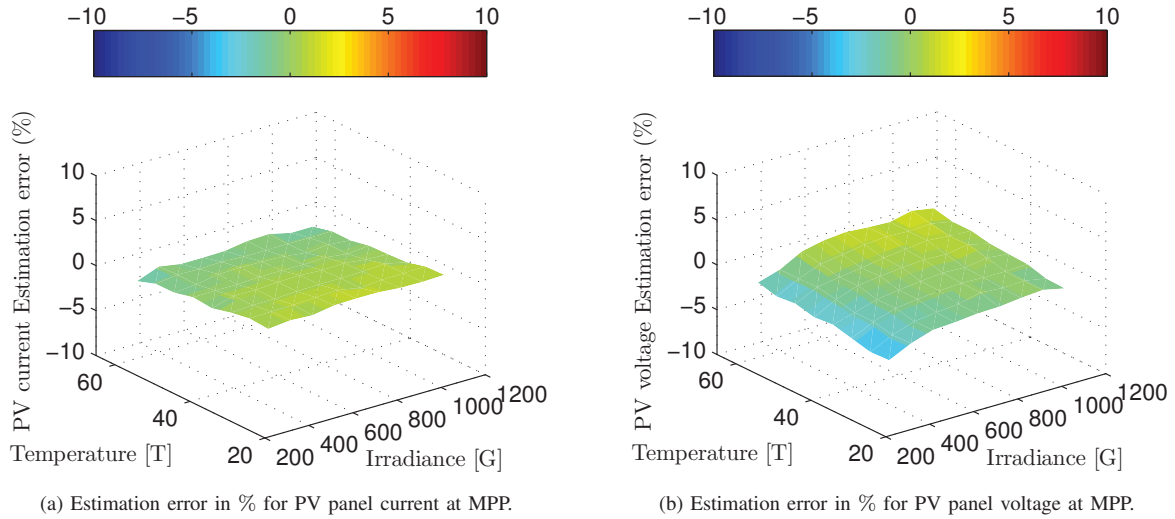
(a) Estimation error in % for PV panel current at MPP.

(b) Estimation error in % for PV panel voltage at MPP.

Fig. 18: Estimation errors with respect to the measured values for operating range of G and T for a PV panel.

of fault types including incipient faults; 2) its framework is converter topology-agnostic and independent of type of PV installation and power conversion architecture; 3) it adds minimal system complexity due to multitasking (i.e. both fault diagnosis and control) of a power converter computing platform. Moreover, the proposed approach is general in the sense that it can be applied to another energy conversion system (e.g. a battery energy system).

APPENDIX A
ESTIMATION ERRORS FOR PV PANEL OPERATING CURRENT AND VOLTAGE AT MPP

Fig. 18a [Fig. 18b] presents the estimation errors with respect to the measured values in the PV panel operating current [voltage] at MPP as a function of operating range of irradiance G and temperature T. The estimation error for a given G and T is computed by subtracting the real PV panel current [voltage] value at MPP from the estimated value by (2) [(3)]. The current-voltage ($I - V$) curves of a crystalline silicon PV panel are measured to obtain the real PV panel values under regulated G and T conditions. It is shown that the estimation errors are well within $\pm 5\%$ envelope. The fault diagnosis approach is immune to these errors due to the careful selection of the threshold values.

APPENDIX B
FAULT SIGNATURE LIBRARY FOR FI IN A PVECU

Table VI presents the fault signature library which is used to identify the fault type in the FI methodology in Section IV-B.

REFERENCES

[1] P. Jain, J. X. Xu, S. K. Panda, J. Poon, C. Spanos, and S. R. Sanders, "Fault diagnosis via PV panel-integrated power electronics," in *2016 IEEE 17th Workshop on Control and Modeling for Power Electronics (COMPEL)*, pp. 1–6, June 2016.

[2] G. R. Walker and P. C. Sernia, "Cascaded DC-DC converter connection of photovoltaic modules," *IEEE Transactions on Power Electronics*, vol. 19, pp. 1130–1139, July 2004.

[3] L. Linares, R. W. Erickson, S. MacAlpine, and M. Brandemuehl, "Improved energy capture in series string photovoltaics via smart distributed power electronics," in *Twenty-Fourth Annual IEEE Applied Power Electronics Conference and Exposition (APEC), 2009.*, pp. 904–910, Feb 2009.

[4] NREL, "Building America case study: Photovoltaic systems with module-level power electronics. Technology solutions for new and existing homes, energy efficiency & renewable energy (EERE)," no. NREL/FS-5500-64876, pp. 1–2, 2015.

[5] U.S. Department of Energy, "Quadrennial technology review - an assessment of energy technologies and research opportunities," 2015.

[6] P. S. Shenoy, K. A. Kim, B. B. Johnson, and P. T. Krein, "Differential power processing for increased energy production and reliability of photovoltaic systems," *IEEE Transactions on Power Electronics*, vol. 28, pp. 2968–2979, June 2013.

[7] O. Carlos, M. Dragan, D. Chris, and M. Luis, "Impact of distributed power electronics on the lifetime and reliability of PV systems," *Progress in Photovoltaics: Research and Applications*, vol. 25, no. 10, pp. 821–835.

[8] M. Kasper, D. Bortis, and J. W. Kolar, "Classification and comparative evaluation of PV panel-integrated DC-DC converter concepts," *IEEE Transactions on Power Electronics*, vol. 29, pp. 2511–2526, May 2014.

[9] A. M. Bazzi, K. A. Kim, B. B. Johnson, P. T. Krein, and A. Dominguez-Garcia, "Fault impacts on solar power unit reliability," in *2011 Twenty-Sixth Annual IEEE Applied Power Electronics Conference and Exposition (APEC)*, pp. 1223–1231, March 2011.

[10] A. Sastry, S. Kulasekaran, J. Flicker, R. Ayyanar, G. TamizhMani, J. Roy, D. Srinivasan, and I. Tilford, "Failure modes and effect analysis of module level power electronics," in *2015 IEEE 42nd Photovoltaic Specialist Conference (PVSC)*, pp. 1–3, June 2015.

[11] M. K. et al., "Assessment of photovoltaic module failures in the field," in *International Energy Agency, Photovoltaic Power Systems Programme*, May 2017.

[12] R. J. Patton, P. M. Frank, and R. N. Clarke, *Fault Diagnosis in Dynamic Systems: Theory and Application*. Upper Saddle River, NJ: Prentice-Hall, Inc., Oct. 1989.

[13] E. Ribeiro, A. J. M. Cardoso, and C. Boccaletti, "Fault-tolerant strategy for a photovoltaic DC–DC converter," *IEEE Transactions on Power Electronics*, vol. 28, pp. 3008–3018, June 2013.

[14] E. Jamshidpour, P. Poure, and S. Saadate, "Photovoltaic systems reliability improvement by real-time FPGA-based switch failure diagnosis and fault-tolerant DC-DC converter," *IEEE Transactions on Industrial Electronics*, vol. 62, pp. 7247–7255, Nov 2015.

[15] J. Poon, P. Jain, I. C. Konstantakopoulos, C. Spanos, S. K. Panda, and S. R. Sanders, "Model-based fault detection and identification for switching power converters," *IEEE Transactions on Power Electronics*, vol. 32, pp. 1419–1430, Feb 2017.

[16] K. A. Kim, G. S. Seo, B. H. Cho, and P. T. Krein, "Photovoltaic hot-spot detection for solar panel substrings using AC parameter charac-

TABLE VI
FAULT SIGNATURE LIBRARY

Fault type	Fault event	Fault magnitude ($\frac{1}{\xi(t)}$)	Fault signature ($\mathbf{f}_i$)
PV panel faults			
$i=1$	Soiling, Continuous mild partial shading, Mild cells breakage, EVA browning	$\frac{\Delta I_{pv}^{ref} G\left(1+K_i(T-T^{ref})\right)}{G^{ref}}$	$[0,0,1,0]^T$
$i=2$	Bypass diode failures, Continuous severe partial shading, Severe cells breakage	$\frac{\Delta V_{pv}^{ref}\left(1+K_p(T-T^{ref})\right)}{1+K_i(T-T^{ref})}$	$[0,0,0,1]^T$
$i=3$	Interconnect faults, PID, Faults related to PV shunt and series resistances	$\left\{\left(\frac{\Delta I_{pv}^{ref} G\left(1+K_i(T-T^{ref})\right)}{G^{ref}}\right)^2 + \left(\frac{\Delta V_{pv}^{ref}\left(1+K_p(T-T^{ref})\right)}{1+K_i(T-T^{ref})}\right)^2\right\}^{\frac{1}{2}}$	$\xi\left[0,0,\frac{\Delta I_{pv}^{ref} G\left(1+K_i(T-T^{ref})\right)}{G^{ref}},\frac{\Delta V_{pv}^{ref}\left(1+K_p(T-T^{ref})\right)}{1+K_i(T-T^{ref})}\right]^T$
Power converter faults			
$i=4$	Open switch fault in SW_1	$\left\{\left(\frac{i_{load}(t)}{D_{s_3}}\right)^2 + \left(\frac{R*i_{load}(t)-D_{s_1}*D_{s_3}*v_{pv}(t)}{D_{s_3}^2}\right)^2 + \left(\frac{I_{pv}^{ref} G\left(1+K_i(T-T^{ref})\right)}{G^{ref}}\right)^2 + \left(\frac{V_{pv}^{ref}\left(1+K_p(T-T^{ref})\right)}{1+K_i(T-T^{ref})}-V_{oc}\right)^2\right\}^{\frac{1}{2}}$	$\xi\left[\frac{i_{load}(t)}{D_{s_3}},-\frac{R*i_{load}(t)-D_{s_1}*D_{s_3}*v_{pv}(t)}{D_{s_3}^2},\frac{I_{pv}^{ref} G\left(1+K_i(T-T^{ref})\right)}{G^{ref}},\frac{V_{pv}^{ref}\left(1+K_p(T-T^{ref})\right)}{1+K_i(T-T^{ref})}-V_{oc}\right]^T$
$i=5$	Short switch fault in SW_1	$\left\{\left(\frac{i_{load}(t)}{D_{s_3}}-i_L(t)\right)^2 + \left(\frac{I_{pv}^{ref} G\left(1+K_i(T-T^{ref})\right)}{G^{ref}}-i_{pv}(t)\right)^2 + \left(\frac{V_{pv}^{ref}\left(1+K_p(T-T^{ref})\right)}{1+K_i(T-T^{ref})}-v_{pv}(t)\right)^2\right\}^{\frac{1}{2}}$	$\xi\left[\frac{i_{load}(t)}{D_{s_3}}-i_L(t),0,\frac{I_{pv}^{ref} G\left(1+K_i(T-T^{ref})\right)}{G^{ref}}-i_{pv}(t),\frac{V_{pv}^{ref}\left(1+K_p(T-T^{ref})\right)}{1+K_i(T-T^{ref})}-v_{pv}(t)\right]^T$
$i=6$	Open switch fault in SW_2	$\left\{\left(\frac{i_{load}(t)}{D_{s3}}-i_L(t)\right)^2 + \left(\frac{R*i_{load}(t)-D_{s1}*D_{s3}*v_{pv}(t)}{D_{s3}^2}\right)^2 + \left(\frac{I_{pv}^{ref} G\left(1+K_i(T-T^{ref})\right)}{G^{ref}}-i_{pv}(t)\right)^2 + \left(\frac{V_{pv}^{ref}\left(1+K_p(T-T^{ref})\right)}{1+K_i(T-T^{ref})}-v_{pv}(t)\right)^2\right\}^{\frac{1}{2}}$	$\xi\left[\frac{i_{load}(t)}{D_{s3}}-i_L(t),-\frac{R*i_{load}(t)-D_{s1}*D_{s3}*v_{pv}(t)}{D_{s3}^2},\frac{I_{pv}^{ref} G\left(1+K_i(T-T^{ref})\right)}{G^{ref}}-i_{pv}(t),\frac{V_{pv}^{ref}\left(1+K_p(T-T^{ref})\right)}{1+K_i(T-T^{ref})}-v_{pv}(t)\right]^T$
$i=7$	Short switch fault in SW_2	$\left\{\left(\frac{i_{load}(t)}{D_{s_3}}\right)^2 + \left(\frac{R*i_{load}(t)-D_{s_1}*D_{s_3}*v_{pv}(t)}{D_{s_3}^2}\right)^2 + \left(\frac{I_{pv}^{ref} G\left(1+K_i(T-T^{ref})\right)}{G^{ref}}-I_{sc}\right)^2 + \left(\frac{V_{pv}^{ref}\left(1+K_p(T-T^{ref})\right)}{1+K_i(T-T^{ref})}\right)^2\right\}^{\frac{1}{2}}$	$\xi\left[\frac{i_{load}(t)}{D_{s_3}},-\frac{R*i_{load}(t)-D_{s_1}*D_{s_3}*v_{pv}(t)}{D_{s_3}^2},\frac{I_{pv}^{ref} G\left(1+K_i(T-T^{ref})\right)}{G^{ref}}-I_{sc},\frac{V_{pv}^{ref}\left(1+K_p(T-T^{ref})\right)}{1+K_i(T-T^{ref})}\right]^T$
$i=8$	Open switch fault in SW_3	$\left\{\left(\frac{i_{load}(t)}{D_{s_3}}\right)^2 + \left(\frac{R*i_{load}(t)-D_{s_1}*D_{s_3}*v_{pv}(t)}{D_{s_3}^2}-v_C(t)\right)^2 + \left(\frac{I_{pv}^{ref} G\left(1+K_i(T-T^{ref})\right)}{G^{ref}}\right)^2 + \left(\frac{V_{pv}^{ref}\left(1+K_p(T-T^{ref})\right)}{1+K_i(T-T^{ref})}-V_{oc}\right)^2\right\}^{\frac{1}{2}}$	$\xi\left[\frac{i_{load}(t)}{D_{s_3}},-\frac{R*i_{load}(t)-D_{s_1}*D_{s_3}*v_{pv}(t)}{D_{s_3}^2}-v_C(t),\frac{I_{pv}^{ref} G\left(1+K_i(T-T^{ref})\right)}{G^{ref}},\frac{V_{pv}^{ref}\left(1+K_p(T-T^{ref})\right)}{1+K_i(T-T^{ref})}-V_{oc}\right]^T$
$i=9$	Short switch fault in SW_3	$\left\{\left(\frac{i_{load}(t)}{D_{s_3}}-i_L(t)\right)^2, + \left(\frac{I_{pv}^{ref} G\left(1+K_i(T-T^{ref})\right)}{G^{ref}}-i_{pv}(t)\right)^2 + \left(\frac{V_{pv}^{ref}\left(1+K_p(T-T^{ref})\right)}{1+K_i(T-T^{ref})}-v_{pv}(t)\right)^2\right\}^{\frac{1}{2}}$	$\xi\left[\frac{i_{load}(t)}{D_{s_3}}-i_L(t),0,\frac{I_{pv}^{ref} G\left(1+K_i(T-T^{ref})\right)}{G^{ref}}-i_{pv}(t),\frac{V_{pv}^{ref}\left(1+K_p(T-T^{ref})\right)}{1+K_i(T-T^{ref})}-v_{pv}(t)\right]^T$

TABLE VI: *CONTINUED FROM PREVIOUS PAGE*

Fault type	Fault event	Fault magnitude ($\frac{1}{\xi}$)	Fault signature ($\mathbf{f}_i$)
Power converter faults			
$i = 10$	Open switch fault in SW_4	$\left\{ \left(\frac{(1-D_{s_3})*i_{load}(t)}{D_{s_3}}\right)^2 + \left(\frac{D_{s_3}^2 v_{pv}(t)+R*i_{load}(t)-D_{s_1}*D_{s_3}*v_{pv}(t)}{D_{s_3}^2}\right)^2 + \left(\frac{I_{pv}^{ref}G\left(1+K_i(T-T^{ref})\right)}{G^{ref}} - i_{pv}(t)\right)^2 + \left(\frac{V_{pv}^{ref}\left(1+K_p(T-T^{ref})\right)}{1+K_i(T-T^{ref})} - v_{pv}(t)\right)^2 \right\}^{\frac{1}{2}}$	$\xi \left[\begin{array}{c} \frac{(1-D_{s_3})*i_{load}(t)}{D_{s_3}}, \\ \frac{-D_{s_3}^2 v_{pv}(t)-R*i_{load}(t)+D_{s_1}*D_{s_3}*v_{pv}(t)}{D_{s_3}^2}, \\ \frac{I_{pv}^{ref}G\left(1+K_i(T-T^{ref})\right)}{G^{ref}} - i_{pv}(t), \\ \frac{V_{pv}^{ref}\left(1+K_p(T-T^{ref})\right)}{1+K_i(T-T^{ref})} - v_{pv}(t) \end{array} \right]^{T}$
$i = 11$	Short switch fault in SW_4	$\left\{ \left(\frac{i_{load}(t)}{D_{s_3}} - i_L(t)\right)^2 + \left(\frac{R*i_{load}(t)-D_{s_1}*D_{s_3}*v_{pv}(t)}{D_{s_3}^2}\right)^2 + \left(\frac{I_{pv}^{ref}G\left(1+K_i(T-T^{ref})\right)}{G^{ref}} - I_{sc}\right)^2 + \left(\frac{V_{pv}^{ref}\left(1+K_p(T-T^{ref})\right)}{1+K_i(T-T^{ref})}\right)^2 \right\}^{\frac{1}{2}}$	$\xi \left[\begin{array}{c} \frac{i_{load}(t)}{D_{s_3}} - i_L(t), \\ -\frac{R*i_{load}(t)-D_{s_1}*D_{s_3}*v_{pv}(t)}{D_{s_3}^2}, \\ \frac{I_{pv}^{ref}G\left(1+K_i(T-T^{ref})\right)}{G^{ref}} - I_{sc}, \\ \frac{V_{pv}^{ref}\left(1+K_p(T-T^{ref})\right)}{1+K_i(T-T^{ref})} \end{array} \right]^{T}$
Electrical sensor faults			
$i = 12$	Fault in $i_L(t)$ sensor	$\Delta c_{12}(t)i_L(t) + \Delta e_{12}(t)$	$[1, 0, 0, 0]^T$
$i = 13$	Fault in $v_C(t)$ sensor	$\Delta c_{13}(t)v_C(t) + \Delta e_{13}(t)$	$[0, 1, 0, 0]^T$
$i = 14$	Fault in $i_{load}(t)$ sensor	$\frac{\Delta c_{14}(t)i_{load}(t)+\Delta e_{14}(t)}{D_{s_3}}\sqrt{1+\left(\frac{R}{D_{s_3}}\right)^2}$	$\frac{1}{\sqrt{1+\left(\frac{R}{D_{s_3}}\right)^2}}[1, -\frac{R}{D_{s_3}}, 0, 0]^T$
$i = 15$	Fault in $v_{pv}(t)$ sensor	$\Delta c_{15}(t)v_{pv}(t) + \Delta e_{15}(t)\sqrt{\left(\frac{D_{s_1}}{D_{s_3}}\right)^2 + 1}$	$\frac{1}{\sqrt{\left(\frac{D_{s_1}}{D_{s_3}}\right)^2+1}}[0, \frac{D_{s_1}}{D_{s_3}}, 0, 1]^T$
$i = 16$	Fault in $i_{pv}(t)$ sensor	$\Delta c_{16}(t)i_{pv}(t) + \Delta e_{16}(t)$	$[0, 0, 1, 0]^T$

I_{sc} = PV panel short circuit current, V_{oc} = PV panel open circuit voltage, D_{s_1} = duty cycle for SW_1, D_{s_3} = duty cycle for SW_3
$\Delta c_i(t)$ = drift in sensor gain, $\Delta e_i(t)$ = offset

terization," *IEEE Transactions on Power Electronics*, vol. 31, no. 2, pp. 1121–1130, 2016.

[17] J. Solrzano and M. A. Egido, "Automatic fault diagnosis in PV systems with distributed MPPT," *Energy Conversion and Management*, vol. 76, pp. 925–934, 2013.

[18] W. Wang, A. C. F. Liu, H. S. H. Chung, R. W. H. Lau, J. Zhang, and A. W. L. Lo, "Fault diagnosis of photovoltaic panels using dynamic Current-Voltage characteristics," *IEEE Transactions on Power Electronics*, vol. 31, pp. 1588–1599, Feb 2016.

[19] M. K. Alam, F. H. Khan, J. Johnson, and J. Flicker, "PV faults: Overview, modeling, prevention and detection techniques," in *2013 IEEE 14th Workshop on Control and Modeling for Power Electronics (COMPEL)*, pp. 1–7, June 2016.

[20] V. Sharma and S. S. Chandel, "Performance and degradation analysis for long term reliability of solar photovoltaic systems: A review," *Renewable and Sustainable Energy Reviews*, vol. 27, pp. 753–767, 2013.

[21] H. Wang, M. Liserre, and F. Blaabjerg, "Toward reliable power electronics: Challenges, design tools, and opportunities," *IEEE Industrial Electronics Magazine*, vol. 7, no. 2, pp. 17–26, 2013.

[22] H. Wang, M. Liserre, F. Blaabjerg, P. de Place Rimmen, J. B. Jacobsen, T. Kvisgaard, and J. Landkildehus, "Transitioning to physics-of-failure as a reliability driver in power electronics," *IEEE Journal of Emerging and Selected Topics in Power Electronics*, vol. 2, no. 1, pp. 97–114, 2014.

[23] S. Yang, D. Xiang, A. Bryant, P. Mawby, L. Ran, and P. Tavner, "Condition monitoring for device reliability in power electronic converters: A review," *IEEE Transactions on Power Electronics*, vol. 25, no. 11, pp. 2734–2752, 2010.

[24] "SunSpec logging in SolarEdge inverters," Technical Documentation, SolarEdge, July 2016.

[25] "Enlighten manager for Solar Professionals," Features Sheet, Enphase, 2017.

[26] E. H. Glaessgen and D. S. Stargel, "The digital twin paradigm for future NASA and U.S. air force vehicles," in *53rd AIAA/ASME/ASCE/AHS/ASC Structures, Structural Dynamics and Materials Conference - Special Session on the Digital Twin, Honolulu, HI, United States*, p. 20120008178, April 2012.

[27] R. K. Hester, C. Thornton, S. Dhople, Z. Zhao, N. Sridhar, and D. Freeman, "High efficiency wide load range buck/boost/bridge photovoltaic microconverter," in *Twenty-Sixth Annual IEEE Applied Power Electronics Conference and Exposition (APEC), 2011*, pp. 309–313, March 2011.

[28] J. G. Kassakian, M. Schlecht, and G. C. Verghese, *Principles of Power Electronics*. Addison-Wesley, 1991.

[29] M. G. Villalva, J. R. Gazoli, and E. R. Filho, "Comprehensive approach to modeling and simulation of photovoltaic arrays," *IEEE Transactions on Power Electronics*, vol. 24, pp. 1198–1208, May 2009.

[30] J. Rosell and M. Ibez, "Modelling power output in photovoltaic modules for outdoor operating conditions," *Energy Conversion and Management*, vol. 47, no. 15, pp. 2424 – 2430, 2006.

[31] W. Luo, Y. S. Khoo, P. Hacke, V. Naumann, D. Lausch, S. P. Harvey, J. P. Singh, J. Chai, Y. Wang, A. G. Aberle, and S. Ramakrishna, "Potential-induced degradation in photovoltaic modules: a critical review," *Energy Environ. Sci.*, vol. 10, pp. 43–68, 2017.

[32] S. Karimi, A. Gaillard, P. Poure, and S. Saadate, "FPGA-based real-time power converter failure diagnosis for wind energy conversion systems," *IEEE Transactions on Industrial Electronics*, vol. 55, pp. 4299–4308, Dec 2008.

[33] A. Youssef, S. El Khil, and I. Slama-Belkhodja, "State observer-based sensor fault detection and isolation, and fault tolerant control of a single-phase PWM rectifier for electric railway traction," *IEEE Transactions on Power Electronics*, vol. 28, pp. 5842–5853, Dec 2013.

[34] S. Nie, X. Pei, Y. Chen, and Y. Kang, "Fault diagnosis of PWM DC-DC converters based on magnetic component voltages equation," *IEEE Transactions on Power Electronics*, vol. 29, pp. 4978–4988, Sept 2014.

Palak Jain (S'15) received her B.E. degree in electrical engineering from Delhi College of Engineering, University of Delhi, India in 2012. She is currently working on her Ph.D with the Department of Electrical and Computer Engineering, National University of Singapore, Singapore. Her research lies at the intersection of power electronics, cyber-physical systems, responsive and resilient energy systems, identification, estimation and learning techniques. She has held R&D positions with Xilinx Research Labs, Solar Energy Research Institute of Singapore, and University of California, Berkeley. Prior to her doctoral studies, she has worked and managed various power plant projects, both thermal and solar PV based at National thermal power Corporation (NTPC) Ltd., India. Ms. Palak is a recipient of a Best Paper Award at 2016 IEEE Workshop on Control and Modeling for Power Electronics, a General Manager Meritorious Award from NTPC Ltd., the Chief Minister's Gold Medal for the best undergraduate student, and the D. V. Kohli Gold Medal for the best electrical engineer from Delhi college of Engineering, University of Delhi, India.

Jason Poon (S'11) received the B.S. degree from the Olin College of Engineering, Needham, MA, USA, in 2012, and the M.S. degree from the University of California, Berkeley, CA, USA, in 2015, both in electrical engineering. He is currently working toward the Ph.D. degree with the Department of Electrical Engineering and Computer Sciences, University of California, Berkeley. He has held R&D positions with Dialog Semiconductor, ABB Corporate Research, the National Renewable Energy Laboratory, the Massachusetts Institute of Technology, the National University of Singapore, and Typhoon HIL. His research interests include the design, control, and optimization of power electronics circuits and systems. Mr. Poon is a recipient of the National Science Foundation Graduate Research Fellowship, the National Defense Science and Engineering Graduate Fellowship, and a Best Paper Award at the 2016 IEEE Workshop on Control and Modeling for Power Electronics for his work on distributed fault-tolerant power electronics.

Jai Prakash Singh is heading Advance PV Module Technology team at Solar Energy Research Institute of Singapore (SERIS). In 2015, he received his PhD degree in Electrical and Computer Engineering from National University of Singapore. He also holds M.Tech degree in Energy Science and Engineering from Indian Institute of Technology (IIT) Bombay, Mumbai and B.Tech degree in Electrical Engineering from Jamia Millia Islamia University, New Delhi. Jai Prakash has more than 10 years of experience on c-Si solar cell and module R&D. In 2008, he joined Moser Baer Photovoltaic as senior R&D engineer and in 2010, he joined PV module group at the SERIS. His research work focuses on advance PV module development, bifacial device characterization, simulation & loss analysis, failure analysis and reliability study of c-Si PV modules, Building-Integrated PV, smart module concepts and PV recycling.

Costas Spanos (M'87–SM'92–F'98) received the EE Diploma from the National Technical University of Athens, Greece in 1980 and the M.S. and Ph.D. degrees in ECE from Carnegie Mellon University in 1981 and 1985, respectively. In 1988 he joined the Faculty at the department of Electrical Engineering and Computer Sciences of the University of California, Berkeley. He has served as the Director of the Berkeley Microlab, the Associate Dean for Research in the College of Engineering and as the Chair of the Department of EECS. He works in statistical analysis in the design and fabrication of integrated circuits, and on novel sensors and computer-aided techniques in semiconductor manufacturing. He also works on statistical data mining techniques for energy efficiency applications. He has participated in two successful startup companies, Timbre Tech, (acquired by Tokyo Electron) and OnWafer Technologies (acquired by KLA-Tencor). He is presently the Director of the Center of Information Technology Research in the Interest of Society (CITRIS) and the Chief Technical Officer for the Berkeley Educational Alliance for Research in Singapore (BEARS).

Seth R. Sanders (S'88–M'88–SM'08–F'10) is Professor in the Department of Electrical Engineering and Computer Sciences at the University of California, Berkeley. He received B.S. degree (1981) in Electrical Engineering and Physics, and the M.S. (1985) and Ph.D. (1989) degrees in Electrical Engineering from the Massachusetts Institute of Technology, Cambridge. Following an early experience as a Design Engineer at the Honeywell Test Instruments Division in 1981-83, he joined the UC Berkeley faculty in 1989. Dr. Sanders technical interests are in electrical energy and power conversion systems . Dr. Sanders is presently or has recently been active in supervising research projects in the areas of flywheel energy storage, electric machine design, renewable energy systems, integrated power conversion circuits, and IC designs for power conversion applications. Dr. Sanders is co-founder and CTO of Amber Kinetics, Inc., a technology developer, manufacturer, and project developer of utility scale flywheel energy storage systems. During the 1992-1993 academic year, he was on industrial leave with National Semiconductor, Santa Clara, CA. Dr. Sanders received the NSF Young Investigator Award and multiple Best Paper Awards from the IEEE Power Electronics and the IEEE Industry Applications Societies. He has served as Chair of the IEEE PELS Technical Committee on Computers in Power Electronics, Chair of the IEEE PELS Technical Committee on Power Conversion Components and Systems, and as Member-At-Large of the IEEE PELS Adcom. He is an IEEE Fellow, a Distinguished Lecturer of the IEEE PELS and IAS societies, and recipient of the IEEE PELS Modeling and Control Technical Achievement Award.

Sanjib Kumar Panda (S'86-M'91-SM'01) received the B.Eng. degree from the South Gujarat University, Surat, India, in 1983, the M.Tech. degree from the Indian Institute of Technology, Banaras Hindu University, Varanasi, India, in 1987, and the Ph.D. degree from the University of Cambridge, Cambridge, U.K., in 1991, all in electrical engineering. Since 1992, he has been holding a Faculty Position in the Department of Electrical and Computer Engineering, National University of Singapore, Singapore, and currently serving as an Associate Professor and the Director of the Power & Energy Research Area. He has published more than 200 peer reviewed research papers, coauthored one book and contributed to several book chapters, and six patents. His research interests include high-performance control of motor drives and power electronic converters, condition monitoring and condition based maintenance, building energy efficiency, etc. Dr. Panda received the Cambridge-Nehru Scholarship and M. T. Mayer Graduate Scholarship during his Ph.D. study (1987-1991). He is serving as an Associate Editor of several IEEE Transactions and the Editor of the Journal of Power Electronics, South Korea. He has served in various capacities for the two key conferences IEEE Power Electronics and Drive Systems Conference and IEEE International Conference on Sustainable Energy Technologies Conference series organized and managed by the IEEE Joint Industry Applications Society/ Power Electronics Society (PELS) Society Chapter, Singapore Section. He has served the IEEE Section Congress 2014 as a member of the Program Committee. He is serving as the IEEE R-10 Asia Pacific Liaison Officer for the IEEE PELS. He has received the IEEE Third Millennium Medal, the IEEE Singapore Section Outstanding Volunteer Award in 2010, and the IEEE Region-10 Outstanding Volunteer Award in 2014.